Treatment of acoustic fluid–structure interaction by localized Lagrange multipliers and comparison to alternative interface-coupling methods

Michael R. Ross [a,*], Michael A. Sprague [b], Carlos A. Felippa [c], K.C. Park [c]

[a] Analytical Structural Dynamics Department, Sandia National Laboratories, P.O. Box 5800, MS 0346, Albuquerque, NM 87185-0346, USA
[b] School of Natural Sciences, University of California, P.O. Box 2039, Merced, CA 95344, USA
[c] Department of Aerospace Engineering Sciences and Center for Aerospace Structures, University of Colorado, Campus Box 429, Boulder, CO 80309, USA

ARTICLE INFO

ABSTRACT

This paper is a sequel on the topic of localized Lagrange multipliers (LLM) for applications of fluid–structure interaction (FSI) between finite-element models of an acoustic fluid and an elastic structure. The prequel paper formulated the spatial-discretization methods, the LLM interface treatment, the time-marching partitioned analysis procedures, and the application to 1D benchmark problems. Here, we expand on formulation aspects required for successful application to more realistic 2D and 3D problems. Additional topics include duality relations at the fluid–structure interface, partitioned vibration analysis, reduced-order modeling, handling of curved interface surfaces, and comparison of LLM with other coupling methods. Emphasis is given to non-matching fluid–structure meshes. We present benchmark examples that illustrate the benefits and drawbacks of competing interface treatments. Realistic application problems involving the seismic response of two existing dams are considered. These include 2D modal analyses of the Koyna gravity dam, transient-response analyses of that dam with and without reduced-order modeling, incorporation of nonlinear cavitation effects, and the 3D transient-response analysis of the Morrow Point arch dam.

Published by Elsevier B.V.

1. Introduction

The prequel [35] to this paper presents the underlying theory and analytical formulation for the first application of the method of localized Lagrange multipliers (LLM) to treat the interaction between acoustic-fluid and elastic-structure finite-element (FE) models. That material includes proof-of-concept 1D examples with known analytical solutions. No realistic benchmark application examples were discussed, since those demand coverage of modeling with computer implementation and verification aspects that would have lengthened and diluted the exposition. The present paper addresses that gap. A methodology overview is given next in the interest of self-sufficiency.

The LLM treatment introduces a *kinematic frame* at the fluid–structure interface. Two multiplier fields separately connect the frame to the fluid on one side and to the structure "wet surface" on the other. Both multiplier spaces are discretized as delta functions collocated at the fluid-interface and wet-surface structural nodes. These can be physically interpreted as interaction point forces.

The main goal of this new interface treatment is *complete decoupling* of fluid and structure models, in the sense that those can be constructed separately by different teams, or with different mesh generators. Consequently, finite-element meshes will not necessarily match over the interface. This separation streamlines preprocessing in design stages where one of the models, such as the structure, is modified (e.g. by a design team) while the other is fixed. Or, conversely, the fluid level could be changing while the structure is fixed, as in reservoir filling or pumping operations. Full decoupling also simplifies the production and use of reduced-order models.

A second key goal is to allow *processing by different programs*. For dynamic analysis by direct time integration, this is achieved by combining the LLM method with a partitioned solution procedure. The solution state is advanced separately on each program. These programs exchange information through the interface as they advance in time. The advancing sequence used here departs from the well known predictor-based staggered schemes introduced in [27]; in that, the interface state is solved *implicitly* for frame accelerations and multiplier forces. The latter are back-substituted into the fluid and structure solvers as if they were produced by an external force field. The stability analysis presented in the prequel paper shows that if the same A-stable integration

* Corresponding author. Tel.: +1 505 844 8526.
  E-mail addresses: mross@sandia.gov, mross10b@mac.com (M.R. Ross).

scheme, such as the trapezoidal rule, is chosen for the fluid and structure with identical timesteps, the coupled system retains unconditional stability. One obvious generalization pertains to the use of different time-integration schemes for the fluid and structure, e.g. implicit in the structure and explicit in the fluid for resolving cavitation. In such cases, solutions may not necessarily match in time either.

While the LLM method can provide modeling flexibility, new challenges may be introduced. Even if separate non-interacting models are satisfactory as regards to stability and accuracy, the introduction of interaction can have adverse effects on the coupled response. Furthermore, if the coupled components have widely different physical characteristics (stiffness, mass, etc.), the coupled system may be scale-mismatched by orders of magnitude. This can worsen the condition number of the algebraic interface system and produce unacceptable errors, particularly under long-term cyclic loading. Accuracy monitoring requires measures to assess interface-energy conservation, whereas ill-conditioning effects may be alleviated through multiplier scaling. Error measuring is one of the practical implementation aspects omitted in the prequel paper but covered here.

To assess the LLM treatment, as well as two competing methods (Mortar and direct force–motion transfer) a realistic benchmark application class is chosen: concrete dams subject to seismic excitation. The computational models represent three physical components: structure, soil and fluid. The structure and soil are formulated as displacement-based elasticity energy equations, which are discretized as conventional solid elements. The reservoir water is modeled as a linear acoustic fluid since no significant flow develops during the response timespan of interest. The displacement potential is chosen as the response variable of the governing fluid equations. This choice has the advantage of reducing the number of degrees of freedom to one per node while automatically enforcing irrotationality.

Two actual dam–reservoir configurations are studied: the Koyna gravity dam in Maharashtra, India, and the Morrow Point arch dam in Colorado, USA. A 2D plane-strain model is used for the former and a 3D model is used for the latter. Both configurations involve the interaction of the structure, near-field soil and entrained fluid. Silent boundaries are used to truncate the fluid and soil meshes. In the gravity-dam example, the analysis optionally includes inertial cavitation. This is a highly nonlinear phenomenon whereupon the water elastic modulus drops to near zero in the cavitation volume, and re-pressurizes producing traveling closure shocks. The gravity-dam problem is used also to illustrate the analysis of coupled-system vibrations and the construction and performance of reduced-order dynamic models.

In addition to the two dam configurations, two additional benchmark problems are included. First, the problem of Chopra [7], which involves the 2D interaction of an unbounded acoustic medium with a rigid wall (with prescribed motion) is used to validate the pressure calculations and the silent boundary. Second, the Bleich and Sandler [6] 1D fluid–structure interaction (FSI) problem is used to validate the cavitation treatment.

2. Localized Lagrange multipliers

2.1. Equations of motion

Finite-element discretization of a linear acoustic fluid coupled to an elastic structure with the interface treated by the LLM method yields the following semi-discrete matrix equations of motion (EOM) in terms of displacements and interface forces as discussed in [35] (damping and silent boundaries omitted for brevity):

$$
\begin{bmatrix} \mathbf{M}_S & 0 & 0 & 0 & 0 \\ 0 & \mathbf{M}_F & 0 & 0 & 0 \\ 0 & 0 & 0 & 0 & 0 \\ 0 & 0 & 0 & 0 & 0 \\ 0 & 0 & 0 & 0 & 0 \end{bmatrix} \begin{Bmatrix} \ddot{\mathbf{u}}_S \\ \ddot{\mathbf{u}}_F \\ \ddot{\lambda}_S \\ \ddot{\lambda}_F \\ \ddot{\mathbf{u}}_B \end{Bmatrix}
$$
$$
+ \begin{bmatrix} \mathbf{K}_S & 0 & \mathbf{B}_{Sn} & 0 & 0 \\ 0 & \mathbf{K}_F & 0 & \mathbf{B}_{Fn} & 0 \\ \mathbf{B}_{Sn}^T & 0 & 0 & 0 & -\mathbf{L}_{Sn} \\ 0 & \mathbf{B}_{Fn}^T & 0 & 0 & -\mathbf{L}_{Fn} \\ 0 & 0 & -\mathbf{L}_{Sn}^T & -\mathbf{L}_{Fn}^T & 0 \end{bmatrix} \begin{Bmatrix} \mathbf{u}_S \\ \mathbf{u}_F \\ \lambda_S \\ \lambda_F \\ \mathbf{u}_B \end{Bmatrix} = \begin{Bmatrix} \mathbf{f}_S \\ \mathbf{f}_F \\ 0 \\ 0 \\ 0 \end{Bmatrix}. \tag{1}
$$

For the structure model, $\mathbf{u}_S$ is the array of structural node displacements, whereas $\mathbf{M}_S, \mathbf{K}_S$ and $\mathbf{f}_S$ denote the master mass matrix, stiffness matrix and applied-force vector, respectively, associated with $\mathbf{u}_S$. For the fluid model, $\mathbf{u}_F$ is the array of fluid node displacements, whereas $\mathbf{M}_F, \mathbf{K}_F$ and $\mathbf{f}_F$ denote the master mass matrix, stiffness matrix and applied-force vector, respectively, associated with $\mathbf{u}_F$. Over the LLM-treated FSI interface, $\mathbf{u}_B$ is the array of frame-node displacements, λ_S is the array of frame-to-structure interaction forces at wet structural nodes, λ_F is the array of frame-to-fluid interaction forces at fluid nodes, $\mathbf{B}_{Sn}$ and $\mathbf{B}_{Fn}$ are Boolean matrices that map λ_S and λ_F onto the full set of structure and fluid node forces, respectively, $\mathbf{L}_{Sn}$ and $\mathbf{L}_{Fn}$ are matrices that map frame displacements $\mathbf{u}_B$ to structure node freedoms and fluid node freedoms, respectively. Structure and fluid nodes need not coincide over the interface. A superposed dot denotes differentiation with respect to time, t.

Fluid irrotationality is enforced by the transformation $\mathbf{u}_F = \mathbf{D}_F \psi$, where ψ collects displacement potential degrees of freedom at fluid mesh nodes; $\mathbf{D}_F$ is a generally rectangular transformation matrix. (Since the displacement potential is a scalar field, there is only one ψ freedom per node.) A congruential transformation on fluid freedoms yields

$$
\begin{bmatrix} \mathbf{M}_S & 0 & 0 & 0 & 0 \\ 0 & \mathbf{M}_{F\psi} & 0 & 0 & 0 \\ 0 & 0 & 0 & 0 & 0 \\ 0 & 0 & 0 & 0 & 0 \\ 0 & 0 & 0 & 0 & 0 \end{bmatrix} \begin{Bmatrix} \ddot{\mathbf{u}}_S \\ \ddot{\psi} \\ \ddot{\lambda}_S \\ \ddot{\lambda}_F \\ \ddot{\mathbf{u}}_B \end{Bmatrix}
$$
$$
+ \begin{bmatrix} \mathbf{K}_S & 0 & \mathbf{B}_{Sn} & 0 & 0 \\ 0 & \mathbf{K}_{F\psi} & 0 & \mathbf{B}_{F\psi n} & 0 \\ \mathbf{B}_{Sn}^T & 0 & 0 & 0 & -\mathbf{L}_{Sn} \\ 0 & \mathbf{B}_{F\psi n}^T & 0 & 0 & -\mathbf{L}_{Fn} \\ 0 & 0 & -\mathbf{L}_{Sn}^T & -\mathbf{L}_{Fn}^T & 0 \end{bmatrix} \begin{Bmatrix} \mathbf{u}_S \\ \psi \\ \lambda_S \\ \lambda_F \\ \mathbf{u}_B \end{Bmatrix} = \begin{Bmatrix} \mathbf{f}_S \\ \mathbf{f}_{F\psi} \\ 0 \\ 0 \\ 0 \end{Bmatrix}, \tag{2}
$$

in which $\mathbf{M}_{F\psi} = \mathbf{D}_F^T \mathbf{M}_F \mathbf{D}_F, \mathbf{K}_{F\psi} = \mathbf{D}_F^T \mathbf{K}_F \mathbf{D}_F, \mathbf{B}_{F\psi n} = \mathbf{D}_F^T \mathbf{B}_{Fn}$ and $\mathbf{f}_{F\psi} = \mathbf{D}_F^T \mathbf{f}_F$, where this equation corresponds to Eq. (22) in [35].

2.2. Reduced-order modeling

The reduced-order model (ROM) formulation considered here reduces the number of normal coordinates by truncating modes of the *uncoupled* problems. The resultant free-vibration eigenproblems, both of generalized symmetric type, are

$$
\mathbf{K}_S \mathbf{v}_{Si} = \omega_{Si}^2 \mathbf{M}_S \mathbf{v}_{Si}, \ (i = 1, \dots, m_S), \quad \mathbf{K}_{F\psi} \mathbf{v}_{Fi} = \omega_{Fi}^2 \mathbf{M}_{F\psi} \mathbf{v}_{Fi},
$$
$$
(i = 1, \dots, m_F). \tag{3}
$$

(The left system in (3) is sometimes called the *dry-structure* eigenproblem.) The eigenvectors are mass orthonormalized. The retained "dry" eigenvectors for the structure are $\mathbf{v}_{Si}, (i = 1, \dots, k_S, k_S < m_S)$, which are collected as columns of matrix $\mathbf{\Phi}_{Sr}$. The retained eigenvectors for the fluid are $\mathbf{v}_{Fi}, (i = 1, \dots, k_F, k_F < m_F)$, which are

collected as columns of matrix $\mathbf{\Phi}_{F\psi r}$. The corresponding normal coordinates $q_i(t)$ and $\varphi_i(t)$ are collected in vectors $\mathbf{q}_r$ and $\boldsymbol{\varphi}_r$, respectively. The truncated expansions of the uncoupled structure and fluid state vectors are

$$\mathbf{u}_{Sr}(t) = \sum_i^{k_S} \mathbf{v}_{Si} q_i(t) = \mathbf{\Phi}_{Sr}\mathbf{q}_r(t), \quad \boldsymbol{\psi}_r(t) = \sum_i^{k_F} \mathbf{v}_{F\psi}\varphi_i(t) = \mathbf{\Phi}_{F\psi r}\boldsymbol{\varphi}_r(t). \tag{4}$$

Inserting these into the semi-discrete equations of motion (2) and performing the change of basis yields

$$\begin{bmatrix} \mathbf{I} & \mathbf{0} & \mathbf{0} & \mathbf{0} & \mathbf{0} \\ \mathbf{0} & \mathbf{I} & \mathbf{0} & \mathbf{0} & \mathbf{0} \\ \mathbf{0} & \mathbf{0} & \mathbf{0} & \mathbf{0} & \mathbf{0} \\ \mathbf{0} & \mathbf{0} & \mathbf{0} & \mathbf{0} & \mathbf{0} \\ \mathbf{0} & \mathbf{0} & \mathbf{0} & \mathbf{0} & \mathbf{0} \end{bmatrix} \begin{Bmatrix} \ddot{\mathbf{q}}_r \\ \ddot{\boldsymbol{\varphi}}_r \\ \ddot{\boldsymbol{\lambda}}_S \\ \ddot{\boldsymbol{\lambda}}_F \\ \ddot{\mathbf{u}}_B \end{Bmatrix}$$
$$+ \begin{bmatrix} \mathbf{\Lambda}_{Sr} & \mathbf{0} & \mathbf{\Phi}_{Sr}^T\mathbf{B}_{Sn} & \mathbf{0} & \mathbf{0} \\ \mathbf{0} & \mathbf{\Lambda}_{F\psi r} & \mathbf{0} & \mathbf{\Phi}_{F\psi r}^T\mathbf{B}_{F\psi n} & \mathbf{0} \\ \mathbf{B}_{Sn}^T\mathbf{\Phi}_{Sr} & \mathbf{0} & \mathbf{0} & \mathbf{0} & -\mathbf{L}_{Sn} \\ \mathbf{0} & \mathbf{B}_{F\psi n}^T\mathbf{\Phi}_{F\psi r} & \mathbf{0} & \mathbf{0} & -\mathbf{L}_{Fn} \\ \mathbf{0} & \mathbf{0} & -\mathbf{L}_{Sn}^T & -\mathbf{L}_{Fn}^T & \mathbf{0} \end{bmatrix} \begin{Bmatrix} \mathbf{q}_r \\ \boldsymbol{\varphi}_r \\ \boldsymbol{\lambda}_S \\ \boldsymbol{\lambda}_F \\ \mathbf{u}_B \end{Bmatrix} \tag{5}$$
$$= \begin{Bmatrix} \mathbf{\Phi}_{Sr}^T\mathbf{f}_S \\ \mathbf{\Phi}_{F\psi r}^T\mathbf{f}_{F\psi} \\ \mathbf{0} \\ \mathbf{0} \\ \mathbf{0} \end{Bmatrix},$$

in which $\mathbf{\Lambda}_{Sr} = \mathbf{\Phi}_{Sr}^T\mathbf{K}_S\mathbf{\Phi}_{Sr}$ and $\mathbf{\Lambda}_{Fr} = \mathbf{\Phi}_{F\psi r}^T\mathbf{K}_{F\psi}\mathbf{\Phi}_{F\psi r}$ are diagonal. Inclusion of damping is straightforward. The transient response analysis by direct time integration can be carried out as discussed in [35].

It should be noted that the selection of modes to be retained in (4) may not necessarily fit the usual strategy of keeping all modes below a certain "cutoff" frequency. For example, fluid slosh modes may be of very low frequency but have a negligible effect on the structural response. A robust approach would be to pick selected coupled modes, but this strategy has not been investigated.

2.3. Interface functionals

In the following, the variational framework of [35] is recalled for the reader's convenience. The LLM treatment is analyzed in further detail, ending with interface-energy conservation and patch-test conditions. Two other interface methods developed for coupling non-matching mesh interfaces, the Mortar and direct force–motion transfer (DFMT) methods, are covered in Sections 3.1 and 3.2, respectively, insofar as needed for the application examples of Section 4.

The boolean and connection matrices $\mathbf{B}_{Sn}, \ldots, \mathbf{L}_{Fn}$ in the global stiffness matrix of (1) are obtained from a variational formulation of the interface equations. This has the significant advantage of maintaining symmetry. Consider the fluid–structure boundary Γ_B shown in Fig. 1a. Since an acoustic fluid is inviscid, only the normal displacements u_{Fn} and u_{Sn}, as well as normal tractions t_{Fn} and t_{Sn}, appear in the strong interaction conditions: $u_{Fn} = u_{Sn}$ and $t_{Fn} + t_{Sn} = 0$, illustrated in Fig. 1b and c. (Note that $t_{Fn} = -p_B$, in which p_B is the hydrodynamic fluid pressure on Γ_B, positive if compressive.) Two weak forms, originally proposed for elasticity problems by Prager [31], Pian and Tong [30] and Atluri [2], can be stated in terms of the following interface functionals

$$\Pi_B^M[\lambda_{Bn}] = \int_{\Gamma_B} (u_{Fn} - u_{Sn})\lambda_{Bn}\,d\Gamma,$$
$$\Pi_B^L[\lambda_{Fn}, \lambda_{Sn}, u_{Bn}] = \int_{\Gamma_B} \{(u_{Fn} - u_{Bn})\lambda_{Fn} + (u_{Sn} - u_{Bn})\lambda_{Sn}\}\,d\Gamma, \tag{6}$$

(these correspond to Eqs. (6) and (5), respectively, in [35]). Here, independently varied fields are identified in square brackets on the left-hand side. In Π_B^M, λ_{Bn} is a global Lagrange multiplier function that connects directly the fluid and structure faces, as shown in Fig. 2a. In Π_B^L, λ_{Fn} and λ_{Sn} are localized Lagrange multiplier functions that link the independently varied normal displacement u_{Bn} of a frame introduced between the two partitions, as shown in Fig. 2b. The LLM treatment of the interface is based on Π_B^L whereas the variational-based Mortar method outlined in Section 3.1 derives from Π_B^M. Substituting

$$u_{Bn} \to \frac{1}{2}(u_{Fn} + u_{Sn}), \quad \frac{1}{2}(\lambda_{Fn} - \lambda_{Sn}) \to \lambda_{Bn}, \tag{7}$$

(a) Interface **(b) Normal displacements** **(c) Normal tractions**
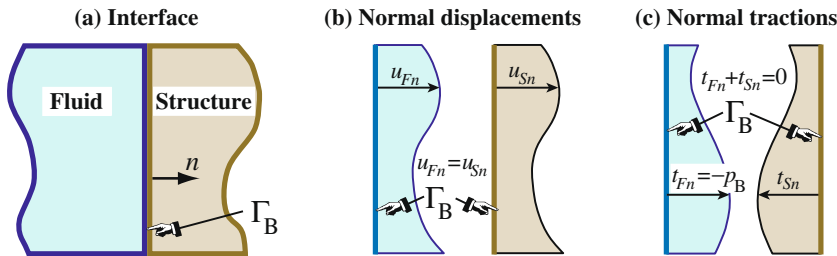
Fig. 1. Fluid–structure interaction on Γ_B: strong interface conditions.

(a) Mortar treatment **(b) LLM treatment**
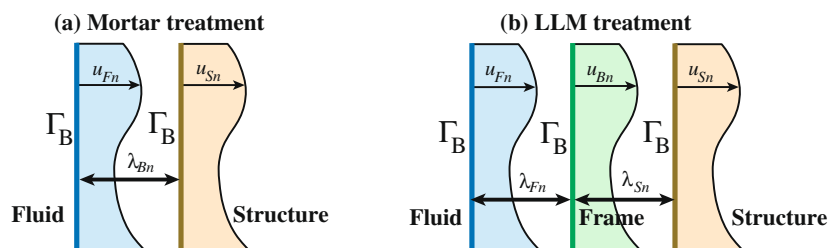
Fig. 2. Weak treatment of fluid–structure interaction using multipliers.

into Π_B^L reduces it to Π_B^M. (The replacements in (7) must be adjusted at "interface crossings" where more than two partitions meet.) Thus, Π_B^L embodies Π_B^M as a special case.

2.4. Discrete interface equations

To produce matrix-connection equations, functionals (6) are discretized by assuming shape functions for the independently varied fields: either λ_{Bn} in Π_B^M, or $\lambda_{Fn}, \lambda_{Sn}$ and u_{Bn} in Π_B^L. Boundary normal displacements u_{Sn} and u_{Fn} come from elements used for the structure and fluid models, respectively, and are prescribed data in both interface functionals (6). Restricting attention to the more general Π_B^L, assume $\lambda_{Fn} = \mathbf{N}_{\lambda F}\lambda_F$, $\lambda_{Sn} = \mathbf{N}_{\lambda S}\lambda_S$ and $u_{Bn} = \mathbf{N}_B\mathbf{u}_B$. For the boundary displacements, take $u_{Fn} = \mathbf{N}_{FB}\mathbf{u}_F$ and $u_{Sn} = \mathbf{N}_{SB}\mathbf{u}_S$, where $\mathbf{N}_{FB}$ and $\mathbf{N}_{SB}$ are shape functions for fluid and structure elements, respectively, evaluated on Γ_B and projected over the normal n. Insert these interpolations into Π_B^L, and integrate over Γ_B to get the discretized functional

$$\Pi_B^L[\lambda_F, \lambda_S, \mathbf{u}_B] = \lambda_F^T(\mathbf{B}_F^T\mathbf{u}_F - \mathbf{L}_F\mathbf{u}_B) + \lambda_S^T(\mathbf{B}_S^T\mathbf{u}_S - \mathbf{L}_S\mathbf{u}_B), \tag{8}$$

in which $\mathbf{B}_F = \int_{\Gamma_B} \mathbf{N}_{FB}^T\mathbf{N}_{\lambda F}\, d\Gamma$, $\mathbf{B}_S = \int_{\Gamma_B} \mathbf{N}_{SB}^T\mathbf{N}_{\lambda S}\, d\Gamma$, $\mathbf{L}_F = \int_{\Gamma_B} \mathbf{N}_{\lambda F}^T\mathbf{N}_B\, d\Gamma$ and $\mathbf{L}_S = \int_{\Gamma_B} \mathbf{N}_{\lambda S}^T\mathbf{N}_B\, d\Gamma$, these are derived in Section 3.5 of [35]. Some notational simplifications have been made in the interest of brevity: subscript n is dropped throughout while Γ_B denotes the discretized interface surface, which may differ from the original one for curved geometries.

The integral evaluations in (6) are greatly simplified by assuming that $\mathbf{N}_{\lambda F}$ and $\mathbf{N}_{\lambda S}$ are *delta functions collocated at the fluid and structure interface nodes*, respectively. If so, $\mathbf{B}_F$ and $\mathbf{B}_S$ become Boolean matrices that select and normal-project node boundary freedoms from the complete state vectors: $\mathbf{u}_{BF} = \mathbf{B}_F^T\mathbf{u}_F$ and $\mathbf{u}_{BS} = \mathbf{B}_S^T\mathbf{u}_S$. The shape functions for $\mathbf{N}_B$ will be piecewise-linear, C^0-continuous, with nodes placed according to distribution rules discussed in [28,29,34,35]. Setting the first variation $\delta\Pi_B = 0$ yields the three matrix equations

$$\mathbf{u}_{BF} = \mathbf{B}_F^T\mathbf{u}_F = \mathbf{L}_F\mathbf{u}_B, \quad \mathbf{u}_{BS} = \mathbf{B}_S^T\mathbf{u}_S = \mathbf{L}_S\mathbf{u}_B, \quad -\mathbf{L}_F^T\lambda_F - \mathbf{L}_S^T\lambda_S = \mathbf{0}. \tag{9}$$

When adjoined to the fluid and structure uncoupled EOMs, these appear as the last 3 rows of the coupled EOM (1) in displacement coordinates. For future use, introduce the matrices

$$\mathbf{Q}_{FF} = \mathbf{L}_F\mathbf{L}_F^T, \quad \mathbf{Q}_{SS} = \mathbf{L}_S\mathbf{L}_S^T, \quad \mathbf{R}_{FF} = \mathbf{L}_F^T\mathbf{L}_F, \quad \mathbf{R}_{SS} = \mathbf{L}_S^T\mathbf{L}_S. \tag{10}$$

Inverses of the $\mathbf{Q}$ and $\mathbf{R}$ matrices appear in ensuing derivations. Since $\mathbf{L}_F$ and $\mathbf{L}_S$ are generally rectangular for non-matching meshes, one or more of (10) could become singular, in which case ordinary inverses do not exist. In the equations below $\mathbf{A}^{-G}$ denotes the Moore-Penrose generalized inverse of $\mathbf{A}$, also popularly known as the pseudoinverse [32].

2.5. Interface force–motion relations

Solving the last equation of (9) by least-squares methods yields

$$\lambda_S = -\mathbf{T}_{SF}\lambda_F, \quad \lambda_F = -\mathbf{T}_{FS}\lambda_S, \tag{11}$$

in which $\mathbf{T}_{SF} = \mathbf{Q}_{SS}^{-G}\mathbf{L}_S\mathbf{L}_F^T$ and $\mathbf{T}_{FS} = \mathbf{Q}_{FF}^{-G}\mathbf{L}_F\mathbf{L}_S^T$ are called *force transfer* matrices. Here pseudoinverses should be replaced by ordinary inverses as appropriate. Products $\mathbf{T}_{FS}\mathbf{T}_{SF}$ and $\mathbf{T}_{SF}\mathbf{T}_{FS}$ are orthogonal projectors. Eliminating $\mathbf{u}_B$ from the first two equations of (9): $\mathbf{u}_{BF} = \mathbf{L}_F\mathbf{u}_B$ and $\mathbf{u}_{BS} = \mathbf{L}_S\mathbf{u}_B$, yields the corresponding transformations between boundary displacement vectors:

$$\mathbf{u}_{BS} = \mathbf{U}_{SF}\mathbf{u}_{BF}, \quad \mathbf{u}_{BF} = \mathbf{U}_{FS}\mathbf{u}_{BS}. \tag{12}$$

Here $\mathbf{U}_{SF} = (\mathbf{L}_S^T)^{-G}\mathbf{R}_{SS}\mathbf{R}_{FF}^{-G}\mathbf{L}_F^T = \mathbf{T}_{FS}^T$ and $\mathbf{U}_{FS} = (\mathbf{L}_F^T)^{-G}\mathbf{R}_{FF}\mathbf{R}_{SS}^{-G}\mathbf{L}_S^T = \mathbf{T}_{SF}^T$ are called *motion transfer* matrices. To prove that $\mathbf{U}_{SF} = \mathbf{T}_{FS}^T$ from linear algebra, start from the identity $\mathbf{R}_{SS}^{-G}\mathbf{L}_S^T = \mathbf{L}_S^T\mathbf{Q}_{SS}^{-G}$, pre-multiply both sides by $\mathbf{L}_F^T(\mathbf{L}_F^T)^{-G}\mathbf{R}_{FF}$ and use projector properties. Likewise for $\mathbf{U}_{FS} = \mathbf{T}_{SF}^T$. The transformation duality (12) can be established more directly from work theorems, noting that no energy is gained or lost at the interface, as follows. The complementary virtual work δW_B^* of interface displacements on their conjugate multiplier variations is

$$\delta W_{BS}^* = \mathbf{u}_{BS}^T\delta\lambda_S, \quad \delta W_{BF}^* = \mathbf{u}_{BF}^T\delta\lambda_F, \quad \delta W_B^* = \delta W_{BF}^* + \delta W_{BS}^* = 0. \tag{13}$$

Setting $\delta\lambda_F = -\mathbf{T}_{FS}\delta\lambda_S$ and $\mathbf{u}_{BS}^T = \mathbf{u}_{BF}^T\mathbf{U}_{SF}^T$ in $\delta W_B^* = 0$ gives $\mathbf{u}_{BF}^T(\mathbf{U}_{SF}^T - \mathbf{T}_{FS})\delta\lambda_S = 0$ for arbitrary $\mathbf{u}_{BF}$ and $\delta\lambda_S$, whence $\mathbf{T}_{FS} = \mathbf{U}_{SF}^T$. Setting $\delta\lambda_S = -\mathbf{T}_{SF}\delta\lambda_F$ and $\mathbf{u}_{BF}^T = \mathbf{u}_{BS}^T\mathbf{U}_{FS}^T$ gives $\mathbf{u}_{BS}^T(\mathbf{U}_{FS}^T - \mathbf{T}_{SF})\delta\lambda_F = 0$ for arbitrary $\mathbf{u}_{BS}$ and $\delta\lambda_F$, whence $\mathbf{T}_{SF} = \mathbf{U}_{FS}^T$.

2.6. Interface patch tests

The duality (12) holds for *any* $\mathbf{L}_F$ and $\mathbf{L}_S$, even if those matrices were filled with random numbers. It is thus independent of the choice of frame discretization, or even of whether a frame is present. This generality can be used to an advantage for other non-matching mesh treatments, e.g. the Mortar and DFMT methods described in Sections 3.1 and 3.2, respectively. The placement of frame nodes may affect, however, the results of the interface patch test (IPT) as shown by the following example, which is a variant of one given in [29].

Consider the two simple non-matching 2D meshes pictured in Fig. 3a. The interface Γ_B of height H connects three bilinear rectangular fluid elements of height $\frac{1}{3}H$ to two bilinear rectangular structural elements of height $\frac{1}{2}H$. All elements have uniform out-of-plane thickness h. Of the four frame nodes, nodes 1 and 4 are placed at both ends and nodes 2 and 3 are symmetrically located at distance αH from the middle structure boundary node as illustrated. Here $-\frac{1}{3} \leqslant \alpha \leqslant \frac{1}{6}$ is a dimensionless free parameter; conventionally $\alpha > 0$ if the middle frame nodes lie in the center thirdspan,
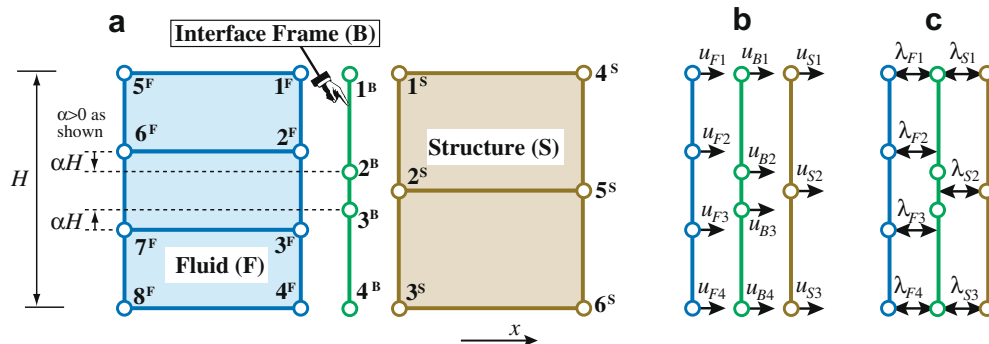
Fig. 3. Example to illustrate interface patch test and the zero-moment rule (ZMR): (a) insertion of interface frame, (b) displacements at interface and (c) localized Lagrange multipliers.

as shown in the figure. If $\alpha = \frac{1}{6}$ frame nodes 2 and 3 coalesce and the frame has 3 nodes. If $\alpha = -\frac{1}{3}$ nodes 2 and 3 coalesce with the end nodes and the frame has 2 nodes. The only displacement degrees-of-freedom (DOF) considered are the interface displacements shown in Fig. 3b. These are collected in vectors

$$\mathbf{u}_{BS}^T = [\, u_{S1} \quad u_{S2} \quad u_{S3} \,], \quad \mathbf{u}_{BF}^T = [\, u_{F1} \quad u_{F2} \quad u_{F3} \quad u_{F4} \,],$$
$$\mathbf{u}_B^T = [\, u_{B1} \quad u_{B2} \quad u_{B3} \quad u_{B4} \,]. \tag{14}$$

The interface multiplier DOF, shown in Fig. 3c, are collected in vectors

$$\boldsymbol{\lambda}_S^T = [\, \lambda_{S1} \quad \lambda_{S2} \quad \lambda_{S3} \,], \quad \boldsymbol{\lambda}_F^T = [\, \lambda_{F1} \quad \lambda_{F2} \quad \lambda_{F3} \quad \lambda_{F4} \,]. \tag{15}$$

The connection and force-transfer matrices for arbitrary α, excluding the node-coalescence cases $\alpha = -\frac{1}{3}$ and $\alpha = \frac{1}{6}$, are

$$\mathbf{L}_F = \begin{bmatrix} 1 & 0 & 0 & 0 \\ \frac{3\alpha}{1+3\alpha} & \frac{1}{1+3\alpha} & 0 & 0 \\ 0 & 0 & \frac{1}{1+3\alpha} & \frac{3\alpha}{1+3\alpha} \\ 0 & 0 & 0 & 1 \end{bmatrix}, \quad \mathbf{L}_S = \begin{bmatrix} 1 & 0 & 0 & 0 \\ 0 & 1/2 & 1/2 & 0 \\ 0 & 0 & 0 & 1 \end{bmatrix},$$

$$\mathbf{T}_{SF} = \begin{bmatrix} 1 & \frac{3\alpha}{1+3\alpha} & 0 & 0 \\ 0 & \frac{1}{1+3\alpha} & \frac{1}{1+3\alpha} & 0 \\ 0 & 0 & \frac{3\alpha}{1+3\alpha} & 1 \end{bmatrix}, \quad \mathbf{T}_{FS} = \frac{1}{2} \begin{bmatrix} 2 & -3\alpha & 0 \\ 0 & 1+3\alpha & 0 \\ 0 & 1+3\alpha & 0 \\ 0 & -3\alpha & 2 \end{bmatrix}. \tag{16}$$

To check the constant-stress interface patch test (IPT), one assumes that the three fluid elements are under uniform pressure p, positive if compression. If displacement shape functions vary linearly along the edge, as in the case of a bilinear fluid element, the consistent interface fluid node forces are $\tilde{\mathbf{f}}_{BF} = -\frac{1}{6} phH[1 \quad 2 \quad 2 \quad 1]^T$. Assuming a similar linear shape function variation over the structural elements and uniform stress $\sigma_{xx} = -p$, others zero, the consistent structural node forces are $\tilde{\mathbf{f}}_{BS} = \frac{1}{4} phH[1 \quad 2 \quad 1]^T$. To apply the IPT, set $\tilde{\lambda}_F = \tilde{\mathbf{f}}_{BF}, \tilde{\lambda}_S = \tilde{\mathbf{f}}_{BS}$ and use the multiplier transformation (11) to compute

$$\boldsymbol{\lambda}_S = -\mathbf{T}_{SF}\tilde{\lambda}_F = \frac{pHh}{6(1+3\alpha)} \begin{bmatrix} 1+9\alpha \\ 4 \\ 1+9\alpha \end{bmatrix}, \quad \boldsymbol{\lambda}_F = -\mathbf{T}_{FS}\tilde{\lambda}_S = -\frac{pHh}{4} \begin{bmatrix} 1-3\alpha \\ 1+3\alpha \\ 1+3\alpha \\ 1-3\alpha \end{bmatrix}. \tag{17}$$

The IPT is passed if $\lambda_S = \tilde{\lambda}_S$ and $\lambda_F = \tilde{\lambda}_F$. Clearly this happens if and only if $\alpha = \frac{1}{9}$. This is the only 4-node-frame configuration that satisfies the zero-moment rule (ZMR) [28,29].

The rigid-motion IPT tests whether a linearly varying fluid boundary displacement field is correctly transmitted to the structure and vice-versa. If d denotes uniform translation along x and θ the rotation about z, the correct node displace-

ment values are $\hat{\mathbf{u}}_{BF} = d[1 \quad 1 \quad 1 \quad 1]^T + \frac{1}{6}\theta H [-3 \quad -1 \quad 1 \quad 3]^T$ and $\hat{\mathbf{u}}_{BS} = d[1 \quad 1 \quad 1]^T + \frac{1}{2}\theta H [-1 \quad 0 \quad 1]^T$. Application of the displacement transformations (12) gives $\mathbf{u}_{BS} = \mathbf{U}_{SF}\hat{\mathbf{u}}_{BF}$ that reproduces $\hat{\mathbf{u}}_{BS}$ exactly for any α. The converse transformation, however, is exact only for $\alpha = \frac{1}{6}$.

3. Alternative interface-coupling methods

3.1. Mortar method

Since its inception in 1990 [5] the Mortar method has gained popularity as an interfacing scheme for multiphysics capable of handling non-matching meshes [3,4,14,39]. With growing acceptance the name has come to designate a set of loosely related mesh-coupling techniques. Their common feature is the use of a single "gluing" Lagrange multiplier field that links directly the two sides of the interface (i.e. without a kinematic frame). For coupling of an inviscid fluid (in particular, an acoustic fluid) to an elastic structure, the gluing field is a scalar (λ_{Bn} in Section 2.3).

Mortar interface equations have been constructed typically from Galerkin or other weighted-residual methods (see e.g. [20]). This is inevitable for general fluid models that are not derivable from variational principles. In the present context we will restrict Mortar interface equations to be based on the functional Π_B^M of (6), a variational framework that preserves symmetry. The only field to be discretized is the scalar multiplier function λ_{Bn} on Γ_B. Physically, this is the normal-to-the-interface surface traction, i.e. wall pressure.

In most of the published literature on Mortar methods, multipliers are distributed functions interpretable as surface tractions. To make a fair comparison with LLM we take the multiplier space for λ_{Bn} to be that of delta functions, as pictured in Fig. 4, which can be viewed as interaction point forces. For an alternative Mortar formulation without the use of delta functions, please see [17,19,40], which is based on discretization spaces for continuous multipliers that are orthogonal to the primal variables allowing an easy condensation of the dual variables.

The key question is: Where should the point forces in our description be placed? For matching meshes, point forces are located at the coincident nodes; see Fig. 4a. For non-matching meshes, e.g. Fig. 4b, there are several reasonable options for point-force locations. One option is to declare either the fluid or structure face as master (typically that pertaining to the finer mesh, as explicitly recommended in Section 4.5.2) and to collocate point forces at the master nodes. This is illustrated in Fig. 4c with the fluid face picked as master. A dual-master scheme (see, e.g. [18]) collocates multipliers at all interface nodes as shown in Fig. 4d; this avoids master vs. slave decisions, but may lead to sin-
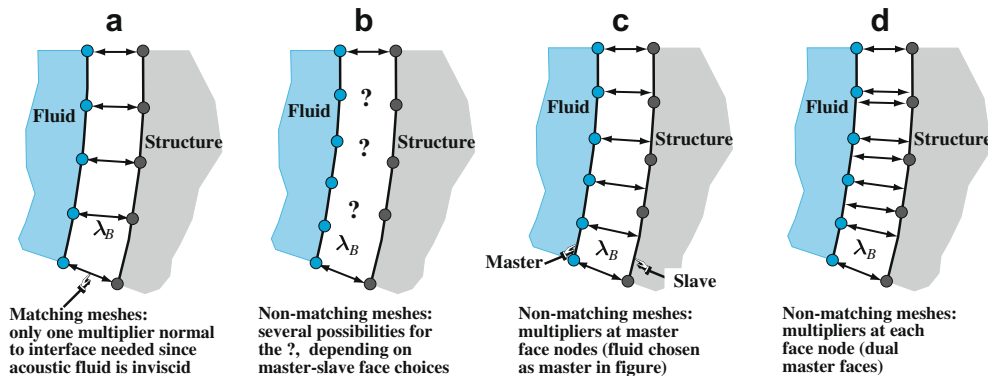
Fig. 4. Mortar interface treatment with node-collocated delta-function multipliers.

M.R. Ross et al./Comput. Methods Appl. Mech. Engrg. 198 (2009) 986–1005

991

gularity or ill-conditioning. Similar freedom placement decisions may be necessary when using distributed Lagrange multiplier spaces. Note that regardless of choice, a master mesh must know about the boundary shape functions of the slave one, and the modularity of the LLM treatment is lost.

3.1.1. Equations of motion

From now on subscript n will be omitted for brevity. With the discrete multiplier assumption written as $\lambda_B = \mathbf{N}_{\lambda B}\lambda_B$, insertion into Π_B^M of (6) gives the discretized functional

$$\Pi_B^M[\lambda_B] = \lambda_B^T(\widehat{\mathbf{B}}_F^T\mathbf{u}_F - \widehat{\mathbf{B}}_S^T\mathbf{u}_S), \tag{18}$$

where $\widehat{\mathbf{B}}_F = \int_{\Gamma_B} \mathbf{N}_{FB}^T\mathbf{N}_{\lambda B}\,d\Gamma$ and $\widehat{\mathbf{B}}_S = \int_{\Gamma_B} \mathbf{N}_{SB}^T\mathbf{N}_{\lambda B}\,d\Gamma$. Since $\mathbf{N}_{\lambda B}$ consists of delta functions, the integrals reduce to collocation on the master face and interpolation on the other. For non-matching meshes $\widehat{\mathbf{B}}_F$ and $\widehat{\mathbf{B}}_S$ are not Boolean and so will differ generally from the $\mathbf{B}_F$ and $\mathbf{B}_S$ of the LLM treatment. Setting $\delta\Pi_B^M = 0$ yields the matrix connection equation $\widehat{\mathbf{B}}_S^T\mathbf{u}_S = \widehat{\mathbf{B}}_F^T\mathbf{u}_F$. For interpretation, let $\mathbf{f}_{BS} = \widehat{\mathbf{B}}_S^T\lambda_B$ and $\mathbf{f}_{BF} = -\widehat{\mathbf{B}}_F^T\lambda_B$ be the boundary force arrays conjugate to $\mathbf{u}_{BS}$ and $\mathbf{u}_{BF}$, respectively. Further, we require that $\mathbf{f}_{BS} + \mathbf{f}_{BF} = \mathbf{0}$, which expresses discrete interface force equilibrium. Adjoining this to the dynamic equations of the uncoupled fluid and structure gives the matrix equations of motion in terms of structural and fluid displacements. If damping is neglected the EOM are

$$\begin{bmatrix} \mathbf{M}_S & \mathbf{0} & \mathbf{0} \\ \mathbf{0} & \mathbf{M}_F & \mathbf{0} \\ \mathbf{0} & \mathbf{0} & \mathbf{0} \end{bmatrix} \begin{Bmatrix} \ddot{\mathbf{u}}_S \\ \ddot{\mathbf{u}}_F \\ \ddot{\lambda}_B \end{Bmatrix} + \begin{bmatrix} \mathbf{K}_S & \mathbf{0} & \widehat{\mathbf{B}}_S^T \\ \mathbf{0} & \mathbf{K}_F & -\widehat{\mathbf{B}}_F^T \\ \widehat{\mathbf{B}}_S & -\widehat{\mathbf{B}}_F & \mathbf{0} \end{bmatrix} \begin{Bmatrix} \mathbf{u}_S \\ \mathbf{u}_F \\ \lambda_B \end{Bmatrix} = \begin{Bmatrix} \mathbf{f}_S \\ \mathbf{f}_F \\ \mathbf{0} \end{Bmatrix}. \tag{19}$$

As before, fluid irrotationality is enforced by the transformation $\mathbf{u}_F = \mathbf{D}_F\psi$, where ψ collects displacement potential degrees of freedom at fluid mesh nodes. Carrying out a congruential transformation on fluid DOF yields

$$\begin{bmatrix} \mathbf{M}_S & \mathbf{0} & \mathbf{0} \\ \mathbf{0} & \mathbf{M}_{F\psi} & \mathbf{0} \\ \mathbf{0} & \mathbf{0} & \mathbf{0} \end{bmatrix} \begin{Bmatrix} \ddot{\mathbf{u}}_S \\ \ddot{\psi} \\ \ddot{\lambda}_B \end{Bmatrix} + \begin{bmatrix} \mathbf{K}_S & \mathbf{0} & \widehat{\mathbf{B}}_S^T \\ \mathbf{0} & \mathbf{K}_{F\psi} & -\widehat{\mathbf{B}}_{F\psi}^T \\ \widehat{\mathbf{B}}_S & -\widehat{\mathbf{B}}_{F\psi} & \mathbf{0} \end{bmatrix} \begin{Bmatrix} \mathbf{u}_S \\ \psi \\ \lambda_B \end{Bmatrix} = \begin{Bmatrix} \mathbf{f}_S \\ \mathbf{f}_{F\psi} \\ \mathbf{0} \end{Bmatrix}, \tag{20}$$

where $\widehat{\mathbf{B}}_{F\psi n} = \mathbf{D}_F^T\mathbf{B}_{Fn}$. A response analysis can be carried out by the partitioned analysis procedure described in [35], where numerical stability is studied in Appendix A.

3.1.2. Interface force–motion relations

As in Section 2.5, a relationship between the fluid boundary displacements $\mathbf{u}_{BF}$ and the structure boundary displacements $\mathbf{u}_{BS}$ can be found on solving $\widehat{\mathbf{B}}_S^T\mathbf{u}_{BS} = \widehat{\mathbf{B}}_F^T\mathbf{u}_{BF}$ by least squares methods. Defining $\widehat{\mathbf{Q}}_{FF} = \widehat{\mathbf{B}}_F\widehat{\mathbf{B}}_F^T$ and $\widehat{\mathbf{Q}}_{SS} = \widehat{\mathbf{B}}_S\widehat{\mathbf{B}}_S^T$ we have

$$\mathbf{u}_{BF} = \widehat{\mathbf{Q}}_{FF}^{-G}\widehat{\mathbf{B}}_F\widehat{\mathbf{B}}_S^T\mathbf{u}_{BS} = \widehat{\mathbf{U}}_{FS}\mathbf{u}_{BS}, \quad \mathbf{u}_{BS} = \widehat{\mathbf{Q}}_{SS}^{-G}\widehat{\mathbf{B}}_S\widehat{\mathbf{B}}_F^T\mathbf{u}_{BF} = \widehat{\mathbf{U}}_{SF}\mathbf{u}_{BF}. \tag{21}$$

The dual force transformations

$$\mathbf{f}_{BS} = \widehat{\mathbf{T}}_{SF}\mathbf{f}_{BF}, \quad \mathbf{f}_{BF} = \widehat{\mathbf{T}}_{FS}\mathbf{f}_{BS}, \tag{22}$$

follow from interface energy conservation as follows. The complementary virtual work δW_B^* over Γ_B is $\delta W_B^* = \mathbf{u}_{BF}^T\delta\mathbf{f}_{BF} + \mathbf{u}_{BS}^T\delta\mathbf{f}_{BS} = \mathbf{u}_{BS}^T[\widehat{\mathbf{U}}_{FS}^T\delta\mathbf{f}_{BF} + \delta\mathbf{f}_{BS}] = \mathbf{u}_{BS}^T[\widehat{\mathbf{U}}_{FS}^T + \widehat{\mathbf{T}}_{SF}]\delta\mathbf{f}_{BF} = \mathbf{u}_{BS}^T[\widehat{\mathbf{U}}_{FS}^T + \widehat{\mathbf{T}}_{SF}]\widehat{\mathbf{B}}_F^T\delta\lambda_B = 0$ for arbitrary $\mathbf{u}_{BS}$ and $\delta\lambda_B$, whence $\widehat{\mathbf{T}}_{SF} = -\widehat{\mathbf{U}}_{FS}^T$. Similarly $\widehat{\mathbf{T}}_{FS} = -\widehat{\mathbf{U}}_{SF}^T$.

3.1.3. Interface patch tests

The Mortar method based on delta-function multipliers (point interaction forces) produces simpler interaction equations than LLM, as a comparison of the coupled EOM (1), (2) versus (19)–(20) makes obvious. For non-matching meshes, forming $\widehat{\mathbf{B}}_F$ and $\widehat{\mathbf{B}}_S$ involves more work than the Boolean $\mathbf{B}_F$ and $\mathbf{B}_S$ since shape-

function interpolation is generally needed in the former, but there is no need for the LLM connection matrices $\mathbf{L}_S$ and $\mathbf{L}_F$. This simplicity, however, is counterbalanced by two features:

(i) The patch test may be violated if collocated face displacements are used.
(ii) Interaction equations become singular at cross points (2D) or cross lines (3D), which are places where multiple interfaces meet.

Weakness (i) is illustrated by the simple 2D example of Fig. 5a. Two 4-node bilinear elements (1) and (2) are connected to a 9-node Lagrangian biquadratic element (3) as shown. All elements are elastic with material and geometric properties as shown. If elements (1) and (2) on one side and (3) on the other are linked by six multipliers λ_{x1} through λ_{y3}, the interface potential with collocated displacements is

$$\Pi_B^M = \lambda_{x1}(u_{x7} - u_{x4}) + \lambda_{y1}(u_{y7} - u_{y4}) + \lambda_{x2}(u_{x8} - u_{x5}) + \lambda_{y2}(u_{y8} - u_{y5}) + \lambda_{x3}(u_{x9} - u_{x3}) + \lambda_{y3}(u_{y9} - u_{y3}). \tag{23}$$

A stress patch test is run on this coupled model by applying constant tractions $q = t_x = 10$ on the y-normal faces, as pictured in Fig. 5b. The computed stresses σ_{xx}, σ_{yy} and σ_{xy} are contour plotted in Fig. 5c. Evidently the patch test is violated; in fact, the error of σ_{xx} reaches ±32%. It can be verified that the displacement patch test is also violated; thus, motion transfer is incorrect. To pass the patch test, it is necessary to pair the multipliers with weighted node displacements, which is contrary to intuition.

Weakness (ii) has no simple cure within the Mortar context and, in fact, does not depend on whether multipliers are distributed or lumped as point forces. This shortcoming does not affect the examples presented later, however, since their interfaces do not exhibit crossing.

3.2. Direct force–motion transfer (DFMT) methods

The term *direct force–motion transfer* (DFMT) is introduced as a collective label for a wide class of interfacing methods with historical and practical importance. Their common feature is that *no additional interface unknowns are introduced*. Boundary forces and displacements (or velocities) are moved directly from fluid to structure and vice-versa. We examine two common DFMT methods, both of which are related to a consistent interpolation approach. It is also discussed how non-DFMT methods, such as Mortar and LLM, can be implemented in a DFMT manner.

3.2.1. DFMT-CFA

Felippa et al. [15] introduced a DFMT method for coupling a structure FE mesh to a matching fluid FE mesh for underwater-shock (UWS) FSI calculations where the fluid is acoustic but subject to cavitation. There, fluid pressures were lumped as nodal forces acting directly (and normally) on structure nodes. Similarly, structure displacements were applied directly to fluid nodes. We refer to this method as DFMT-CFA, since it was implemented into the CFA (cavitation fluid analyzer) code [15]. A similar approach was used in the CASE (cavitating acoustic spectral element) code [36], in coupling fluid spectral finite-elements to a non-matching structure mesh. This latter approach used consistent interpolation (CI) [13], but with quantities averaged over fluid and structure elements to reduce spurious structure oscillations. In a CI coupling method, the structure forcing vector is evaluated using its shape functions; fluid forces are typically interpolated at structure quadrature points. Likewise, interpolated structure displacements are transferred to the fluid mesh.
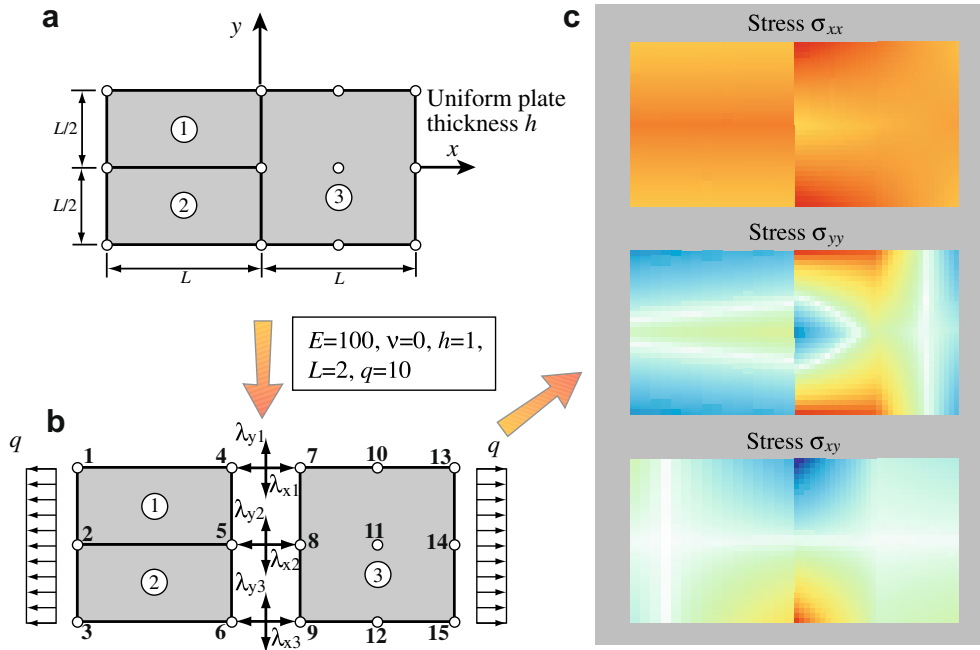
Fig. 5. Patch Test on point-force Mortar treatment of an elasticity problem. (a) Two 4-node bilinear elements connected to a 9-node Lagrangian biquadratic element. (b) Insertion of Mortar Lagrange multipliers. (c) Computed stress contour plot.

3.2.2. Conservative consistent interpolation: DFMT-CCI

While a consistent interpolation approach for coupling non-matching meshes is straightforward, it is demonstrated in [13] that energy may be lost at the interface. While consistent interpolation can be non-conservative, it does not mean that the methods are inaccurate [13], especially for short-duration simulations like those for underwater shock analysis. To address this energy discrepancy, [12,13] modified the standard CI as discussed below; we refer to this approach as DFMT-CCI (conservative consistent interpolation).

As an illustrative example of CCI coupling, consider the system shown in Fig. 3. First, the fluid displacements $\mathbf{u}_{BF}$ are interpolated from structure displacements with the structural element shape functions. The motion transfer matrix in $\mathbf{u}_{BF} = \mathbf{U}_{FS}\mathbf{u}_{BS}$ for the example problem is given by

$$\mathbf{U}_{FS} = \begin{bmatrix} 1 & 0 & 0 \\ \frac{1}{3} & \frac{2}{3} & 0 \\ 0 & \frac{2}{3} & \frac{1}{3} \\ 0 & 0 & 1 \end{bmatrix}. \tag{24}$$

Second, the transformation from fluid to structure forces, $\mathbf{f}_{BS} = \mathbf{T}_{SF}\mathbf{f}_{BF}$, follows from duality: $\mathbf{T}_{SF} = -\mathbf{U}_{FS}^T$. This approach enforces interface energy conservation. The transformation matrix $\mathbf{T}_{SF}$ can be found equivalently by lumping fluid pressures into nodal forces (as discussed in [13]) and calculating the structure force vector consistently. In typical aeroelastic problems the fluid mesh is more refined than the structure. Thus, the DFMT-CCI method interpolates refined mesh values from coarse mesh values, which helps to produce well conditioned coupling matrices.

To check the stress interface patch test, apply uniform pressure p over the 3 fluid elements. Then $\mathbf{f}_{BF} = -\frac{1}{6}phH[1\ \ 2\ \ 2\ \ 1]^T$ and $\mathbf{f}_{BS} = (1/18)phH[5\ \ 8\ \ 5]^T$. Since $\mathbf{f}_{BS} \neq \hat{\mathbf{f}}_{BS} = \frac{1}{4}phH[1\ \ 2\ \ 1]^T$, the test is not passed. Notice that the transformation matrices in (24) are the same as those provided by LLM treatment in the example of Section 2.6 if $\alpha = \frac{1}{6}$. This configuration does not satisfy the ZMR and thus it is not surprising that the stress IPT fails. Applying this method to the example of Fig. 5, in which elements (1) and (2) are taken to be fluid whereas (3) is an elastic solid, shows that the stress IPT is again violated.

3.2.3. DFMT-Mortar and DFMT-LLM

Another subclass of DFMT is that of *global* DFMT methods, which are constructed in two stages. First a multiplier based discretization such as LLM or point-force Mortar is carried out. Interface unknowns are then eliminated by least squares methods as described in Sections 2.5 and 3.1.2 to yield the force transfer matrices $\mathbf{T}_{SF}$ and $\mathbf{T}_{FS}$. The motion transfer matrices follow from duality.

The qualifier *global* indicates that transfer matrices are generally fully populated, meaning that each interface DOF is coupled to every other one. By construction interface energy conservation is satisfied *a priori*, but interface patch tests are not necessarily passed, as previous examples make clear.

Do LLM and DFMT-LLM produce identical results? Only under special conditions. For instance, if connection matrices $\mathbf{L}_F$ and $\mathbf{L}_S$ are square and of full rank. Otherwise, the least-squares elimination of interface unknowns can be expected to work as a filter that projects interface patterns on the column span of the "$\mathbf{Q}$" matrices. This will typically mollify the computed response. A similar remark applies to Mortar versus DFMT-Mortar. Whether this kind of filtering is acceptable or desirable can be expected to be problem dependent.

3.3. Computational cost: LLM vs. DFMT

A simple decision on which method to use can be realized by evaluating the number of steps required in the procedure. In the following, it is assumed that the interface equation has been LU factored. This up-front cost would be similar to the cost of creating the interface transfer matrices for the other methods. It is also assumed that the interface frame is discretized with the same number of degree of freedoms as the refined interface mesh boundary, say the structure N_s. The fluid interface boundary has N_f degrees of freedom. According to [21], the cost (in standard floating-point operation units) of solving a matrix equation with factorization for m time steps is $C = (\frac{1}{2} + m)(N_e)^2$, where N_e is the number of equations. Accordingly, the cost for the interface equation is $C_{LLM} = (\frac{1}{2} + m_l)(2N_s + N_f)^2$. where m_l is the number of time steps for the LLM method.

The cost of using interface transfer matrix operations in each time step would be $C_{DFMT} = m_e(2N_sN_f)$ where m_e is the number of time steps for DFMT. Here, there are two instances in which matrix vector multiplication needs to happen, once for the displacement relation and once for the force relation.

If cavitation effects are not included, then the partitions coupled with LLM may be time-integrated implicitly. Assuming that other partitioned integration procedures use an explicit time integration method with m_e time steps, it is of interest to find out when the LLM method incurs less operations. This leads to $C_{LLM} \leqslant C_{DFMT}$, or

$$m_l(4N_s^2 + 4N_sN_f + N_f^2) + (2N_s^2 + 2N_sN_f + \frac{1}{2}N_f^2) \leqslant 2m_eN_fN_s,$$

$$m_l \leqslant \frac{2m_eN_fN_s}{4N_s^2 + 4N_sN_f + N_f^2} - \frac{1}{2}. \tag{25}$$

As a simplification, if we assume that the number of DOF of the two partitions are the same, then the number of steps for the LLM method should be less than approximately $\frac{2}{9}$ of the time steps of the explicit staggered partitioned procedure: $m_l \leqslant \frac{2}{9}m_e - \frac{1}{2}$. If the DFMT is cheaper, the LLM discretization can be used to handle non-matching meshes to produce the DFMT-LLM transfer matrices.

4. Application problems

4.1. Overview of methods

Table 1 summarizes the labels introduced for interface-coupling methods in the application examples. The methods are listed in order of increasing complexity. The class of DFMT methods has the advantage of not carrying additional interface unknowns during the computations. Mortar introduces one set of multipliers whereas LLM brings two sets of multipliers as well as an interface frame. In comparing the various interface-coupling methods, we consider the following to be desirable attributes:

(1) Passes force and displacement interface patch tests.
(2) Satisfies interface energy conservation conditions.
(3) Maintains full locality of separate meshes.
(4) Provides an error measure for transient analysis.
(5) Properly handles crossing interfaces.

As can be expected, there is a tradeoff between complexity and fulfilling these desirable attributes. The LLM is able to handle all five; it is unknown at this point if the same can be said for DFMT-LLM. However, the importance of these attributes is largely problem dependent. For example, while energy conservation is important in long-term cyclic-type response simulations, it is much less important in early-time calculations such as those in shock-response analysis.

Table 1
Summary of labels used to identify the various interface-coupling methods examined. Methods are listed in order of increasing complexity.

Label	Fluid–structure interface treatment
DFMT-CFA	Local DFMT procedure used in CFA code [15]
DFMT-CCI	Local DFMT based on conservative consistent interpolation [13]
Mortar	Point-force Mortar with transient step-by-step solution of interface equations
DFMT-Mortar	Global DFMT with Mortar-derived transfer matrices (21) and (22)
LLM	LLM with transient step-by-step solution of interface equations
DFMT-LLM	Global DFMT with LLM-derived transfer matrices (11) and (12)

4.2. Time-response error measures

Assessment of the temporal accuracy of the computed response is of interest to compare interface discretization choices. Three error measures are used in our studies:

(1) The comprehensive error factor of Geers [16,36].
(2) Energy balance at the LLM interface frame.
(3) Energy balance between partition boundaries.

These are briefly described in the following subsections.

4.2.1. Comprehensive error factor

The comprehensive error factor [16,36], or C-error, quantifies the error of a transient-response history, called a *candidate solution*, with respect to a benchmark response. The measure is defined as $C = \sqrt{M^2 + P^2}$, in which M is the *magnitude error factor*, which is insensitive to phase discrepancies, and P is the *phase error factor*, which is insensitive to magnitude discrepancies. These are given by

$$M = \sqrt{\vartheta_{cc}/\vartheta_{bb}} - 1, \quad P = \frac{1}{\pi}\arccos\left(\vartheta_{bc}/\sqrt{\vartheta_{bb}\vartheta_{cc}}\right), \tag{26}$$

where

$$\vartheta_{bb} = \frac{1}{t_2 - t_1}\int_{t_1}^{t_2} b^2(t)\,dt, \quad \vartheta_{cc} = \frac{1}{t_2 - t_1}\int_{t_1}^{t_2} c^2(t)\,dt,$$

$$\vartheta_{bc} = \frac{1}{t_2 - t_1}\int_{t_1}^{t_2} b(t)c(t)\,dt. \tag{27}$$

Here $b(t)$ and $c(t)$ are the benchmark and candidate response histories, respectively, and $t \in [t_1, t_2]$ is the time span of interest. Integrals in (27) were evaluated with a composite Simpson's rule.

4.2.2. Interface energy balance error

If the interface is viewed as a closed system, the energy gained (released) on one side of the frame must equal the energy lost (absorbed) by the other side. Consequently, the difference of energies on the two sides of the frame may be used for an error measurement. Two variants of this measure are considered. The first is the difference at the interface proper. At time station $t = t_j$

$$W_{error}^{int}(t_j) = \mathbf{u}_{Bj}^T(-\mathbf{L}_S^T\mathbf{\Lambda}_{Sj} - \mathbf{L}_F^T\mathbf{\Lambda}_{Fj}), \tag{28}$$

in which a j subscript denotes evaluation at time t_j, and a superscript *int* denotes the interface frame. This difference is used to focus on errors associated with the interface equation where Lagrange multipliers are specifically solved. According to the third matrix equation of (9), the coupled system is conservative, since boundary forces are equal and opposite in accordance with Newton's third law. A substantial error indicated by (28) is a sign that the interface matrix is ill-conditioned. A scaling methodology to improve conditioning is discussed in [34].

The second variant is associated with the energy difference evaluated from partition boundary forces and displacements. At time station $t = t_j$

$$W_{error}^{sub}(t_j) = \mathbf{\Lambda}_S^T(\mathbf{B}_{Sj}^T\mathbf{u}_S) + \mathbf{\Lambda}_F^T(\mathbf{B}_{Fj}^T\mathbf{D}_F\boldsymbol{\psi}), \tag{29}$$

where superscript *sub* refers to partition boundaries. This measure assesses energy conservation across the interface and as such is influenced by the interface discretization as well as time integration parameters. Errors associated with the fluid mesh gradient matrix $\mathbf{D}_F$ will also affect this measure. Note that the plus sign is used in (29) because the Lagrange multipliers are equal and opposite at the interface frame.

4.3. 2D model wall-pressure and silent-boundary verification

A key verification of any 2D or 3D FSI code involves pressure-on-wall calculations, since that is a key component of the interaction. Few 2D problems that involve an acoustic fluid have exact analytical solutions for arbitrary base accelerations. The problem shown in Fig. 6a pertains to that rare class. A prismatic rigid dam holds a body of liquid of density ρ_w and constant depth H extending to infinity in the horizontal (x) direction. The ground under the fluid is also rigid. The system is at rest for $t \leqslant 0$. A given horizontal ground acceleration $\ddot{u}_q(t)$ is applied for $t \geqslant 0$. The dynamic pressure field is $p(x, y, t)$ (deviation from the hydrostatic value). The dynamic pressure on the dam wall is $p_{wall}(y, t) = p(0, y, t)$, and we focus on pressure response histories at a distance b from the bottom.

This problem was solved analytically by Chopra [7] for the dam wall pressure $p_{wall}(y, t)$ under the following simplifying assumptions. First, the liquid is acoustic. Second, the effect of the length of the fluid is assumed to be negligible for $L/H > 3$, where L and H are the length and depth of the fluid reservoir, respectively. Finally, the effect of surface waves on p_{wall} may be ignored with little loss of accuracy as long as the depth is greater than about 15 m for a typical ground-motion period. Under these assumptions, the analytical pressure solution is given by the convolution series

$$p_{wall}(y, t) = \frac{4\rho_w c_w}{\pi} \sum_{n=1}^{\infty} \frac{(-1)^{n-1}}{2n-1} \cos(\lambda_n y) \int_0^t \ddot{u}_q(\tau) J_0[\lambda_n c(t-\tau)] \, d\tau, \quad (30)$$

where c_w is the water sound speed, $\lambda_n = (2n-1)\pi/(2H)$ is a wavenumber, and J_0 is the Bessel function of the first kind of order zero. Test data are $\rho_w = 1000$ kg/m^3, $c_w = 1500$ m/s, $H = 80$ m, $b = 40$ m, and the simulation span is $0 \leqslant t \leqslant 8$ s. Finite-element fluid meshes with characteristic element lengths of $L^e = 20$, 10 and 5 m were tested. Fig. 6b shows the coarsest mesh with $L^e = 20$ m. The LLM interface discretization is used, and a plane-wave approximation (PWA) silent boundary truncates the fluid mesh at $L = 300$ m. An acoustic wave travels the domain length (300 m) in only 0.2 s; calculated response histories at the wall can be influenced by reflections from the silent boundary.

The applied acceleration is a digital record of El Centro 1940 earthquake NS horizontal component taken from the COSMOS database [1]. This is shown in Fig. 7a for the first 8 s. Computed responses for the 3 meshes are plotted in Fig. 7b–d, where they are compared with the analytical solution. C-, M- and P-error factors for the LLM-calculated response histories over $0 \leqslant t \leqslant 8$ s are listed at the top of each figure.

We see a clear improvement in LLM-computed responses with decreasing characteristic element length. For the finest mesh, the LLM response agrees well with the analytical solution for $t < 3$ s, but exhibits significant late-time ringing, especially for $t > 5$ s. In order to investigate potential sources for the late-time ringing, we investigate the effectiveness of the PWA and the effects of including fluid damping. Fig. 8a shows the LLM and analytical his-

tories of Fig. 7c along with one calculated with no boundary constraints at the truncated end rather than a PWA. While solutions with and without the PWA show good agreement for $t < 5$ s, there is significantly more late-time ringing in the absence of the PWA. This suggests that calculations may be improved through use of a better silent boundary. Fig. 8b shows the response histories for $L^e = 5$ m calculated with 0.1% stiffness-proportional damping. The response solution is significantly better than that without damping (Fig. 7d); late-time ringing is significantly reduced.

4.4. 1D-model cavitation validation

Under severe ground motions, the effective fluid pressure (hydrostatic plus dynamic) may drop below the water vapor pressure, producing inertial cavitation [10,36]. For a dam under seismic action, the phenomenon is typically triggered by the wet face pulling away from the fluid, which produces a rarefaction wave. As the wave propagates upstream a main cavitation zone develops. The zone eventually collapses on repressurization, producing closure shocks. This event sequence has been reported in several articles and confirmed experimentally [24]. Reference [9] observes that dam stresses may increase by 20–40% from closure shocks. A change of this magnitude in tensile stresses may cause crack growth in a concrete structure.

Within a cavitating volume, the macroscopic bulk modulus K drops to near zero, while the density ρ_w remains sensibly constant, and the pressure stays equal to the vapor pressure. A simple but effective macroscopic constitutive model is a bilinear one, in which $K = 0$ if the effective pressure is less than the vapor pressure, and $K = \rho_w c_w^2$ otherwise. The implementation of this model required extensive changes to the fluid partition solver to handle the nonlinear constitutive behavior. These included modification of element stiffness computations, switching the time integrator to central differences, and injection of appropriate numerical damping to the fluid. The latter item is essential; if damping is not added, spurious numerical oscillations can be observed to break out and quickly fragment the main cavitation zone. This phenomenon, first reported in [23] is termed *frothing*. Technical details may be found in the prequel paper [35]. For reasons of space, only the validation problem is presented here.

The Bleich-Sandler plate problem [6] was used for validation of LLM interface coupling with cavitation. This 1D benchmark problem, defined in Fig. 9a, is the only known nontrivial cavitation FSI problem that possesses an analytical solution, which was obtained with the method of characteristics. A semi-infinite column of acoustic fluid of constant cross section supports a rigid plate of weight W per unit area. An exponentially-decaying pressure wave (defined as shown in the figure) propagates upward through the fluid and impinges on the plate at $t = 0$ triggering a reflected rarefaction wave and cavitation. Properties are as follows: water density $\rho_w = 989$ kg/m^3, sound speed $c_w = 1451$ m/s, gravity $g = 9.81$ m/s^2, plate weight $W = 144.7$ kg/m^2, atmospheric pres-
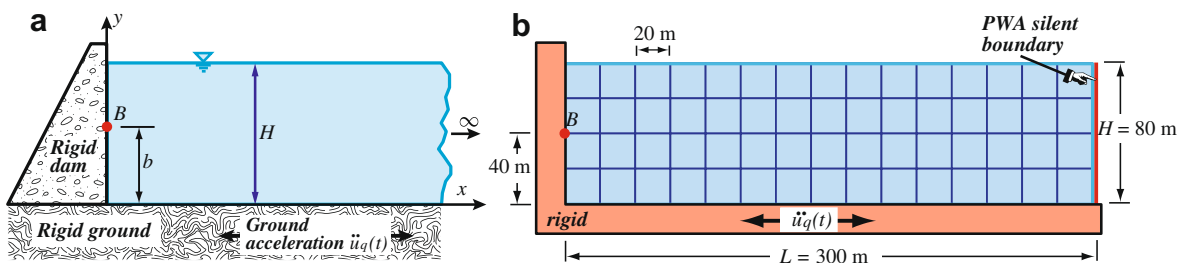
Fig. 6. Rigid dam benchmark problem for pressure-on-wall code verification: (a) cross-section schematic, and (b) discretized fluid.
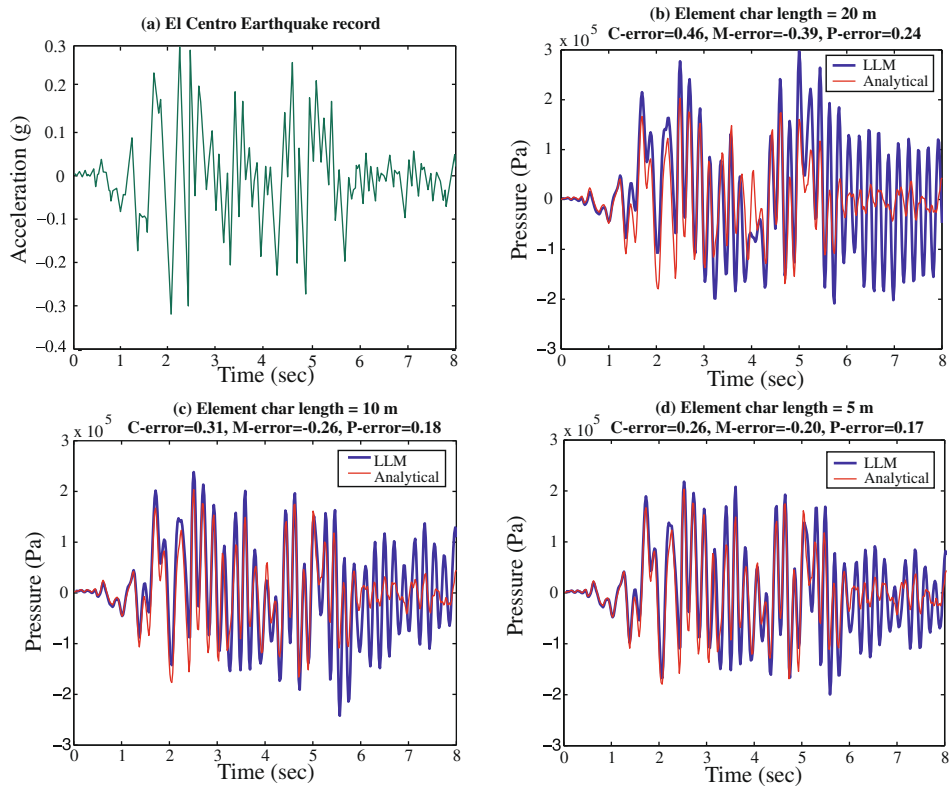
Fig. 7. Rigid dam benchmark problem: (a) base acceleration and (b)–(d) response histories for fluid meshes with three different element sizes.
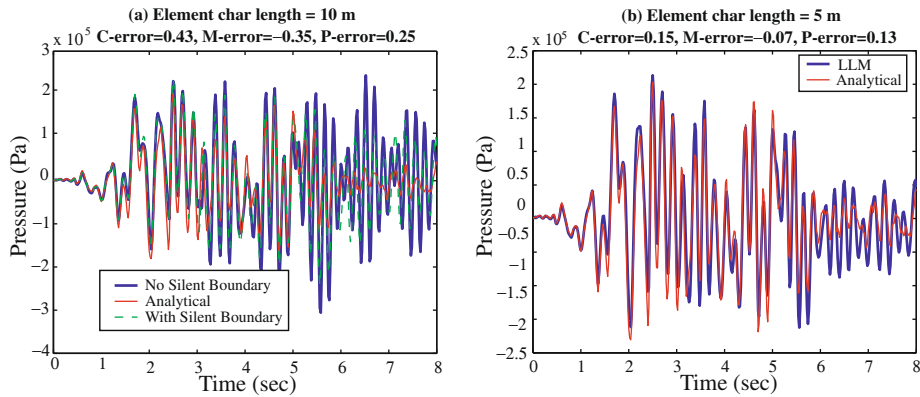
Fig. 8. Rigid dam benchmark: effects of (a) removing silent boundary and (b) adding fluid damping.
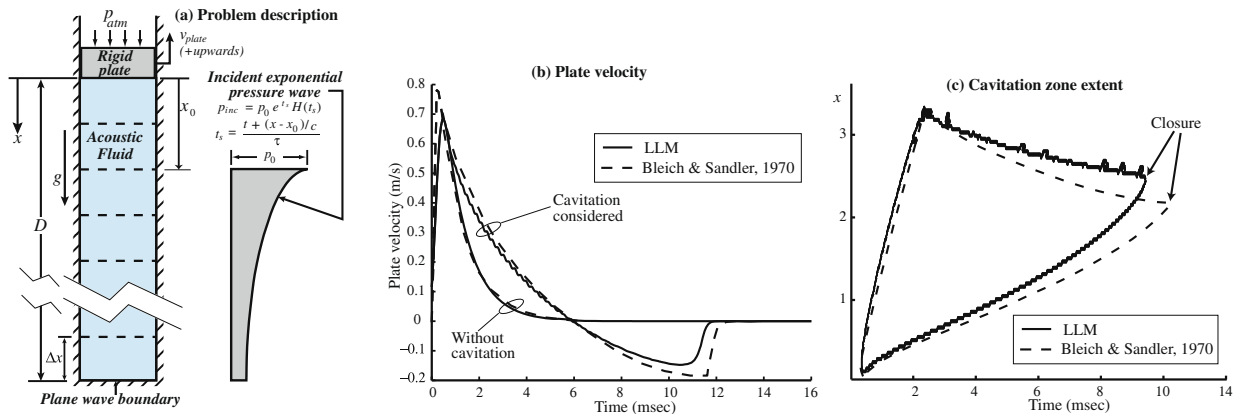
Fig. 9. 1D validation of the cavitation-model implementation with the Bleich and Sandler [6] problem.

sure $p_{atm} = 0.101$ MPa, incident-wavefront pressure $p_0 = 0.710$ MPa and characteristic decay time $\tau = 0.99610^{-3}$ s. With those properties the cavitation zone closes after approximately 11 ms.

The fluid was modeled with 100 2D fluid elements, and was truncated at $D = 3.81$ m with a PWA silent boundary. To suppress frothing, numerical Rayleigh damping with a damping matrix, $\mathbf{C}_{Fd} = \alpha_K \mathbf{K}_{Fd} + \alpha_M \mathbf{M}_{Fd}$, was included in the fluid EOM. Results using the LLM treatment, with damping coefficients $\alpha_K = 10^{-5}$ and $\alpha_M = 0$ are shown in Fig. 9b and c. These results agree with the analytical solution in a manner expected at this fluid refinement level [15].

4.5. 2D analyses: Koyna gravity dam

4.5.1. Model description

Koyna Dam, pictured in Fig. 10a, is a large concrete gravity dam located in Maharashtra, India. Built over 1954–1963, it has a height of 103 m, width of 808 m, volume of 1555 m³ and water storage of 2797 km³. In December 1967 a strong reservoir-induced earthquake shook the dam, which developed large downstream cracks and required major repair work. Ref. [38] remarks: "The event is unique because the Koyna Dam is the only concrete dam to be significantly damaged due to ground shaking." Accordingly, this event has been studied frequently (see, e.g. [8,41]).

Koyna is chosen here as a representative gravity dam. Taking a typical slice in plane strain allows the use of a 2D model, which facilitates detailed parametric studies. Specific study goals include vibration analysis for verifying kinematic continuity, transient analysis with direct time integration, comparison of different interface treatments, transient analysis with reduced-order modeling,

and analysis of the LLM method in the presence of cavitation. Particular attention is given to non-matching meshes throughout.

Fig. 11 shows a representative coarse FE model of the coupled system along with relevant dimensions. Note the use of non-matching meshes at the fluid-solid interface. The dam and the rock foundation are assumed linear elastic, isotropic, and homogeneous. The water is assumed to be acoustic, but cavitation is considered in Section 4.5.6. Both fluid and structure are modeled with four-node quadrilateral elements. Meshes are truncated at non-reflecting boundaries: a PWA silent boundary [34,35] and a viscous-damping boundary (VDB) [22] are employed for the fluid and rock foundation, respectively.

Physical parameters chosen for the system are as follows. For the dam concrete: $E_c = 31.46 \times 10^9$ Pa, $v_c = 0.2$ and $\rho_c = 2690$ kg/m³. For the rock foundation: $E_r = 18 \times 10^9$ Pa, $v_r = 0.2$ and $\rho_r = 1830$ kg/m³. For the reservoir water: $c_w = 1439$ m/s and $\rho_w = 1019$ kg/m³.

4.5.2. Vibration analysis and kinematic continuity

A free-vibration analysis was carried out using the model of Fig. 11. The analysis of free vibrations is accomplished by removing all external applied forces in (2), assuming harmonic motion, and solving the resulting eigenproblem. We note that the global mass matrix in (2) is singular, since the interface DOF have no mass. The associated eigenvalues are infinite and have no physical relevance [33]. Their presence causes no difficulties if an eigensolution procedure such as shifted block Lanczos is used [26]. In addition, the only non-infinity eigenvalues are the combined systems degree of freedoms; not the total of the structure partition plus the fluid partition, as these partitions share some degree of freedoms. These are resolved by the connection and boolean extraction matrices in the global stiffness matrix.

Fig. 12 shows representative mode shapes and associated frequencies with the interface treated with LLM and frame nodes placed to satisfy the ZMR. The lowest frequencies pertain to fluid-surface gravity waves called "sloshing modes" of which the two modes pictured in Fig. 12a and b (6th and 20th, respectively) are typical instances. (Despite their low frequency, sloshing modes have a negligible effect on the structure response.) The spectrum eventually displays more variety with the appearance of acoustic modes, typified by Fig. 12d,f,i and FSI modes, typified by Fig. 12c,e,g,j.

Vibration modes that exhibit strong fluid–structure coupling offer an effective way of visualizing kinematic continuity issues at the fluid–structure interface. Not maintaining kinematic continuity increases the risk for spurious interface energy dissipation [18]. This will be indicated by the interface energy balance errors listed in Section 4.2.2. In the models studied, normal-displacement continuity at the interface was met when the LLM frame was discretized either with nodes placed as per the ZMR, or matching the coarse (structure) mesh nodes. Continuity was vio-
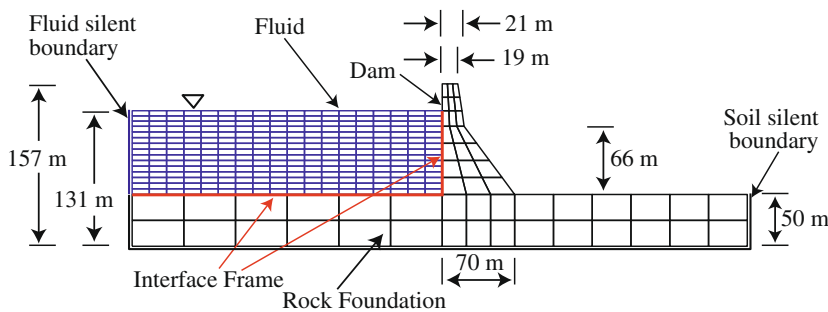
Fig. 11. Representative 2D finite-element model of the Koyna dam–reservoir system.
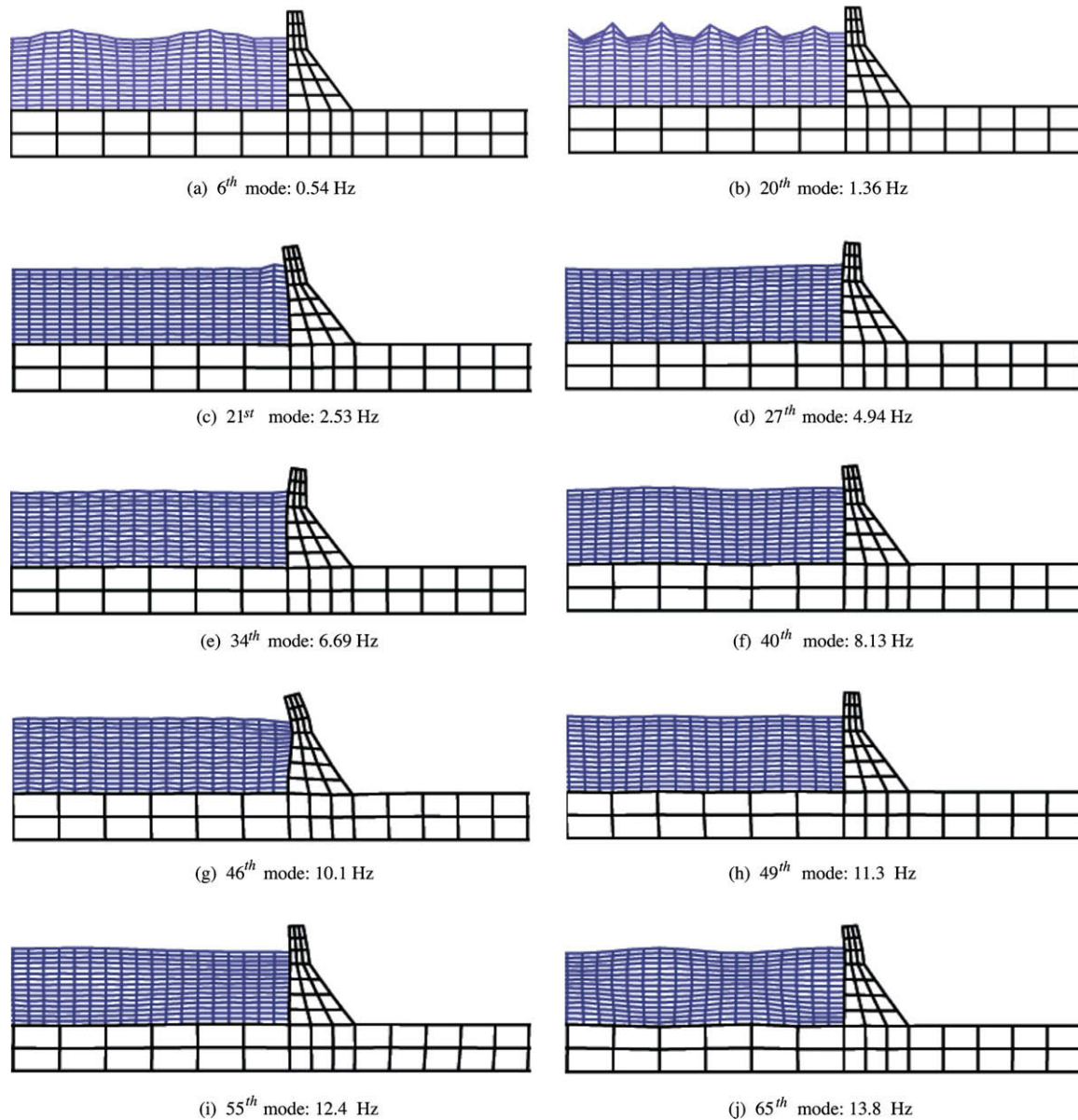
Fig. 12. Representative mode shapes calculated with LLM interface coupling for 10 natural frequencies for the Koyna dam model.

lated for certain meshes when the LLM frame nodes were collocated to coincide with the refined (fluid) mesh nodes. This violation with the interface discretized as the refined mesh occurs when the refined mesh is further refined within a coarse element such that the refined mesh has an integer number of elements ($\geqslant 2$) within one coarse element. At the current time, this has only been studied for linear elements. Fig. 11 depicts a mesh under this condition. Once again, this condition only violates continuity when the refined mesh is chosen as the discretization for the interface.

A vibration analysis with the model of Fig. 11 was then done with point-force Mortar in which multipliers were collocated at nodes of either the coarse (structure) mesh or the fine (fluid) mesh. The governing equations were discussed in Section 3.1.1. The basic findings were:

- Interface kinematic compatibility was verified when the refined mesh was chosen as master. In fact, the vibration results were identical to those produced by LLM with frame nodes collocated at the coarse mesh.

- Interface kinematic compatibility was violated for certain meshes when the coarse mesh was chosen as master. A typical result is pictured in Fig. 13. This violation with the coarse mesh chosen has the master will happen when the refined mesh is further refined within a coarse element; such that the refined mesh has an integer number of elements ($\geqslant 2$) within one coarse element. At the current time, this has only been studied for linear elements.

Reference [18] notes this kind of incompatibility for the Mortar method in the context of structure-structure interaction (SSI). It should be observed that the previous result renders dubious the use of ZMR for point-force Mortar, since that reduces to the coarse-mesh-as-master choice for certain configurations, e.g. that of Fig. 11.

A final comparison was done with the DFMT-CCI interface treatment. A kinematic compatibility violation was discovered when the coarse-mesh displacements were interpolated with the refined-mesh shape functions. This is identical to the results produced by the LLM method when the frame interface nodes are
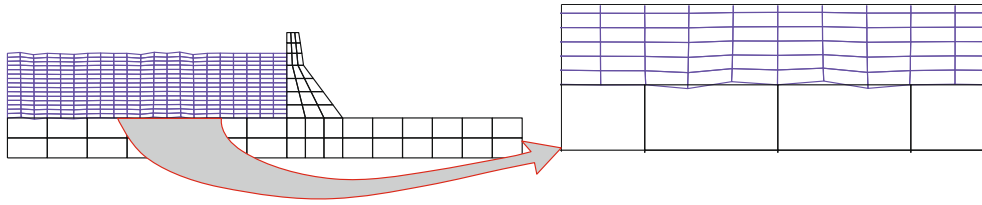
Fig. 13. Representative mode shape calculated with the Mortar method where interface kinematic continuity is violated.

collocated at refined-mesh node locations. The results obtained with DFMT-CCI when the coarse-mesh displacements were interpolated from the refined-mesh displacement were identical to those produced by LLM when frame interface nodes are collocated at refined-mesh node locations. This is not surprising since, in essence, DFMT-CCI is effectively projecting the coarse-mesh displacements onto the finer-mesh ones.

Based on the foregoing findings, we offer the following discretization choice guidelines.

(1) If using point-force Mortar, choose the refined mesh as master.
(2) If using DFMT-CCI, interpolate from the coarse mesh.
(3) If using LLM, collocate frame nodes as per the ZMR or (if that is too demanding) from the coarse mesh. Avoid frame node collocation at refined mesh nodes.

4.5.3. Benchmark transient solution

Passing to response simulations, we seek first to obtain converged benchmark solutions with *matched* meshes for the selected seismic input. Those are used to validate and assess the error involved in using non-matching meshes as well as to study the effect of different interface treatments. For the converged benchmark solution, two interface treatments are considered:

- LLM with frame nodes collocated at matching boundary nodes. Trapezoidal rule (TR) time integration is used for both fluid and structure-soil partitions.
- DFMT-CFA with fluid pressure lumped to structure node forces and structure node motions directly transferred to the matching fluid mesh. Central-difference time integration is used for the fluid whereas the structure-soil partition is integrated by the TR. Identical time increments are used for the partitions.

An acceleration-scaled version of the 1940 El Centro earthquake is chosen as input. The horizontal excitation normal to the dam is taken to be the North-South (180° Component) whereas the vertical excitation is that of the Up Component. Both are taken from the COSMOS database [1]. Unscaled displacement and acceleration records of the NS component are shown in Fig. 14a and b. Its power spectrum (Fig. 14c) illustrates that, for the horizontal acceleration, frequencies below 8 Hz are of concern with a maximum at about 3 Hz. The dominant frequencies in the horizontal direction correspond to the first bending modes of the
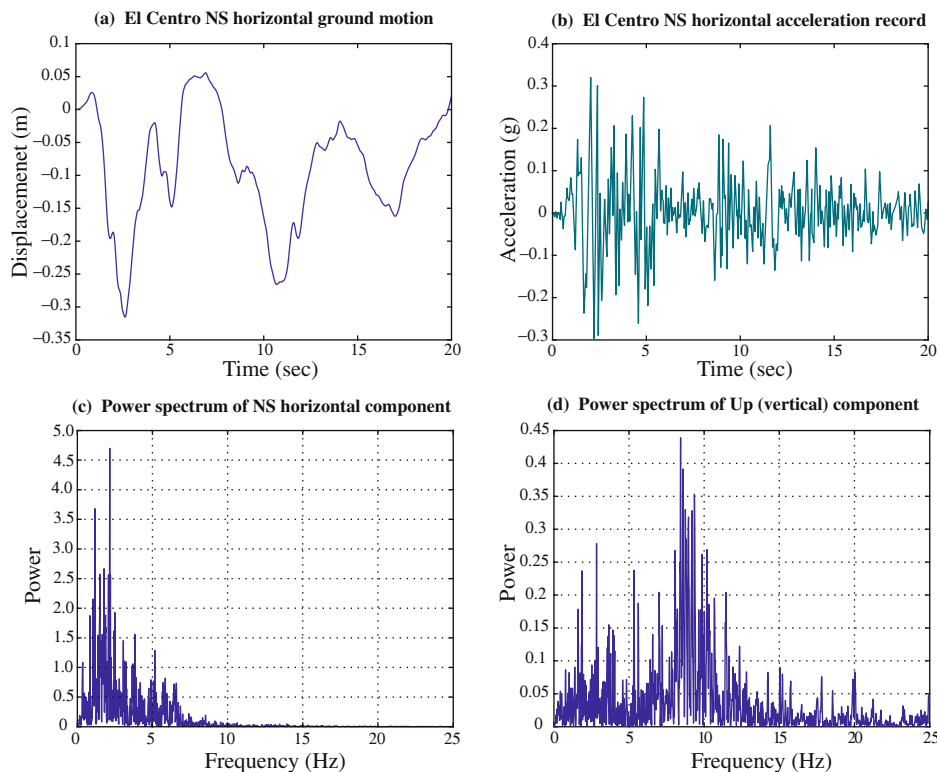
Fig. 14. Selected El Centro earthquake data. For all calculations, acceleration amplitudes were increased by 50%.

dam structure as seen in Fig. 12c–f. Fig. 14d shows that the Up (vertical) acceleration power has a broader frequency range that is significant up to 20 Hz, with a maximum at about 8 Hz. The dominant frequencies in the veritcal direction correspond to vertical motions in the foundation as depicted in Fig. 12g–j. As can be seen, we have selected an earthquake that will significantly excite the structure.

An examination of mode shapes and associated frequencies from Fig. 12 indicates that the dominant horizontal frequency begins to affect the dam–fluid system instead of just the sloshing modes of the fluid, while only the first few dominant modes of the structure are excited. Hence, we chose this particular earthquake as likely to trigger significant FSI effects. The acceleration data, however, is amplified by 50% to emphasize better differences between LLM and other coupling methods.

In both LLM and DFMT-CFA interface treatments, spatial FE meshes were sufficiently refined such that calculated horizontal dam-crest displacements (relative to the base displacement) were insensitive to further mesh refinement. Both methods yielded sufficiently converged solutions with the mesh partially depicted in Fig. 15a. This has a total of 3598 DOF for the coupled system. A time stepsize of 5 ms for the solution calculated with LLM was chosen; solutions were insensitive to further temporal refinement. Alternatively, calculations with DFMT-CFA were restricted by the CFL condition of the central-differences time integration; a time stepsize of 0.1 ms was employed. The DFMT-CFA treatment employs artificial damping as described in [15,36] with coefficient of $\beta = 0.25$ used in this study.

Relative and total horizontal crest displacements are shown in Fig. 15b and c. While differences cannot be seen at plot resolution, the C-error with the DFMT-CFA solution as the benchmark and LLM solution as the candidate is 0.02. A C-error less than 0.1 indicates a good agreement in engineering calculations [16,36].

4.5.4. Non-matching meshes

For the transient analysis with non-matching meshes, three interface treatment methods are explored: LLM, DFMT-LLM and DFMT-Mortar. For LLM and DFMT-LLM, three frame-node collocation variants described below are tried.

A specific example is presented before discussing advantages and disadvantages. The non-matching mesh shown in Fig. 16 is tested. Relative crest displacements are obtained under three variants of the LLM interface treatment in Fig. 17a: frame nodes (i) collocated at refined mesh (fluid) nodes, (ii) at coarse mesh (structure) nodes, and (iii) placed as per the ZMR. C-errors are computed using the converged benchmark response of the DFMT-CFA discussed in Section 4.5.3. The difference between the three variants is small and agreement with the benchmark solution is satisfactory.
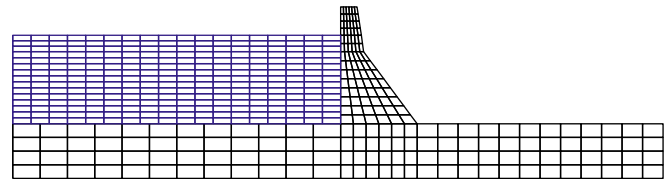
Fig. 16. Example non-matching mesh tested with several interface treatments.

Energy conservation at the fluid–structure interface was checked with the interface error measures introduced in Section 4.2. For the ZMR variant, the average energy error over the 8 s span was 1.16×10^{-7} N m. This is negligible compared to the average total energy on the structural boundary at the interface, which is 6.78×10^{6} N m. The other interface treatments gave similar results. It was found that interface incompatibility was not an issue even when taking the refined mesh as master for this particular mesh. Other meshes did exhibit high energy error at the interface depending on the interface treatment. The only interface treatment that did not have energy conservation issues regardless of the mesh was the ZMR method for the LLM and DFMT-LLM. This is expected due to the findings of kinematic compatibility in Section 4.5.2.

The same model is used with DFMT-LLM, which provides the relative crest displacement history plotted in Fig. 17b. Again the results are similar and are in satisfactory agreement with the benchmark response. Results for the Mortar treatment are shown in Fig. 17c for two choices of master face: refined (fluid) and coarse (structure). No significant differences are observed.

The satisfactory agreement amongst all interface treatments with the benchmark response is a general indication that the interface equations for the example of Fig. 16 are well conditioned. There are situations, however, in which a highly refined mesh is paired with a very coarse mesh. In that case certain master-face choices, such as that of the coarse mesh for the Mortar treatment, may cause kinematic continuity problems as discussed in Section 4.5.2.

The foregoing example is but an instance of a systematic study in which models ranging from roughly 200 to 3500 DOF were run with the various interface treatments. The results of this extensive study are summarized in Fig. 18. Each figure shows the C-error versus the total DOF for a specific treatment. The solid lines are least-squares best-fit exponential functions. Any simulation that exhibited a high interface energy balance error is not included in these results (see Section 4.5.2 for meshes and interface treatments that cause high interface energy balance errors). Clearly, mesh refinement reduces the C-error, since refining the structure has

(a) Converged response mesh (showing portion near dam)

(b) Relative crest motion with respect to base

(c) Total dam crest motion
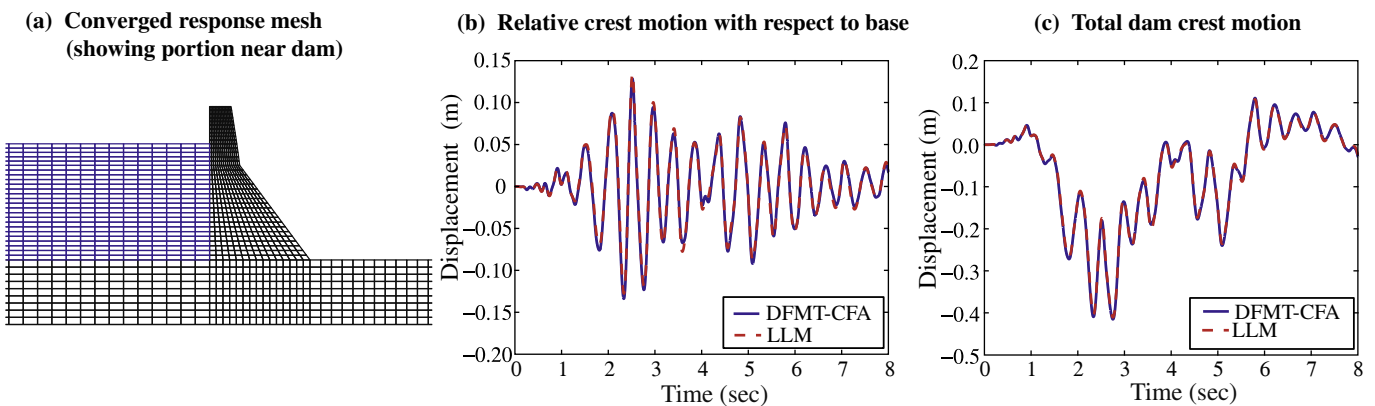
Fig. 15. Benchmark (a) matching FE mesh, and (b), (c) response simulations calculated with LLM and DFMT-CFA interface treatments.

(a) Relative crest motion for LLM interface treatment   **(b) Relative crest motion for DFMT-LLM interface treatment**   **(c) Relative crest motion for DFMT-Mortar interface treatment**
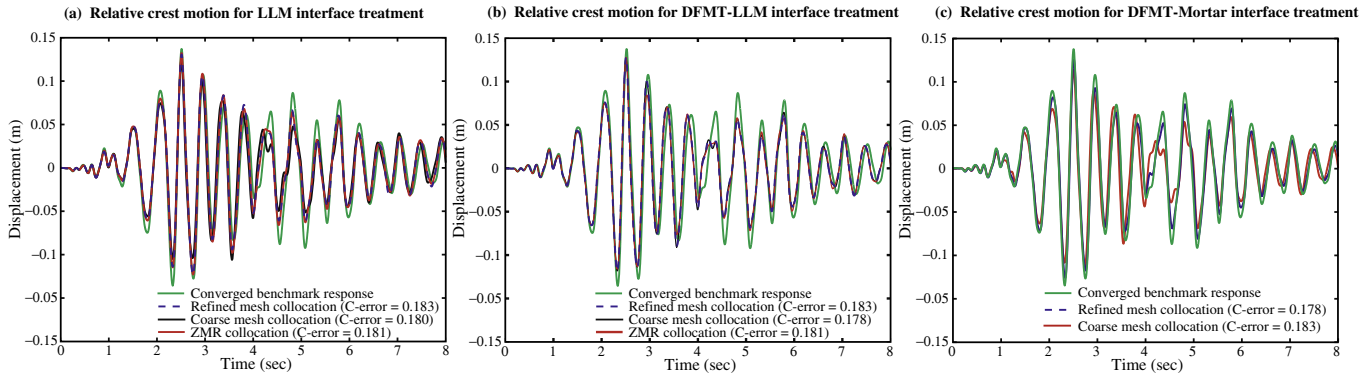
Fig. 17. Dam crest relative-displacement histories for the non-matching mesh model of Fig. 16 with three interface treatments.
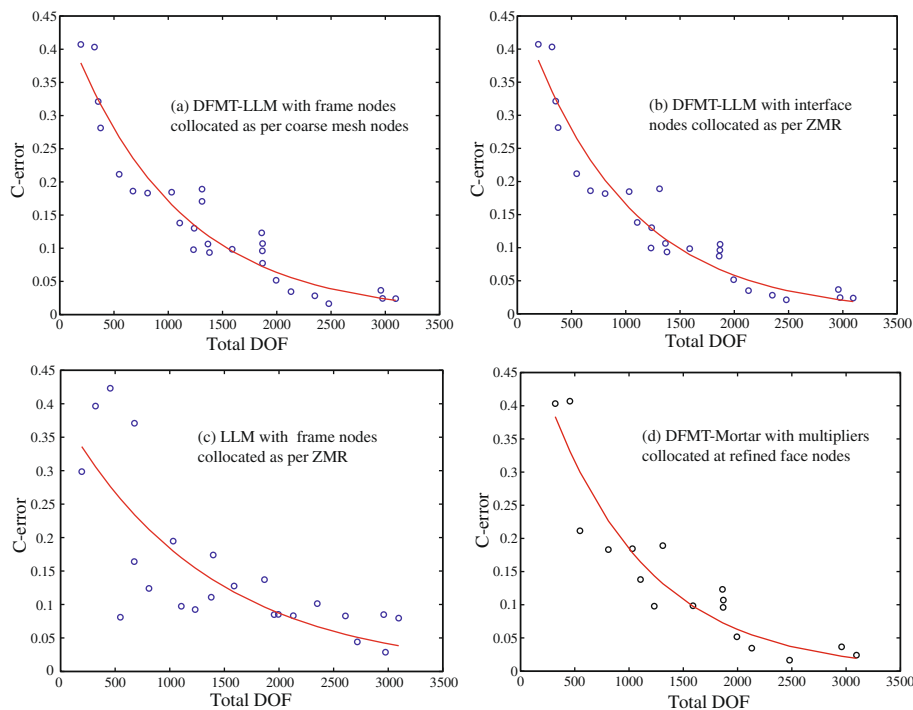
Fig. 18. C-error in terms of total DOF for various interfacing methods. Solid lines are least-squares best-fit exponentials.

more influence on the crest displacement error than refining the fluid, the choice of overall number of DOF for plots can be expected to be only roughly indicative of the general trend. A frequency response analysis indicates that the structure has more influence over the assembled system for the horizontal frequency excitation of the input [34].

4.5.5. Reduced-order modeling

The reduced-order model (ROM) technique explained in Section 2.2 is applied to the non-matching mesh model shown in Fig. 19,
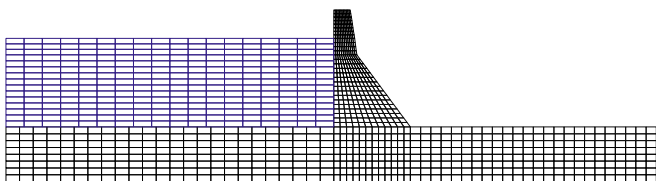
Fig. 19. Example non-matching mesh for ROM evaluation.

using the uncoupled fluid and structure eigenmodes as the basis. The excitation is again the amplified earthquake of Fig. 14.

To evaluate the relative contribution of fluid and structure modes, three reduction schemes were evaluated. Fig. 20a and b shows the C-error of ROM calculated response histories with respect to the benchmark DFMT-CFA history. Here, the horizontal axes indicates the maximum modal frequency, below which all modes are maintained. Fig. 20a shows C-error for responses calculated with all structure modes, but with a subset of fluid modes. Likewise, Fig. 20b shows C-error for responses calculated with all fluid modes, but with a subset of structure modes. Both figures exhibit convergence to the full-model C-error of about 0.06. Clearly, employing fluid and structure modes with frequencies above 40 Hz and 125 Hz, respectively, has little influence on calculated response histories. This is expected as the frequency of the excitation is below 20 Hz. Finally, a transient-response analysis was carried out with reducing both uncoupled structure and fluid eigenvectors to 20% of their original number; this includes fluid and structure modes with frequencies below 15.3 Hz and 111 Hz, respectively. A representative result, plotted

(a) Response C-error for fluid subsystem reduction using all eigenvectors with associated frequency less than or equal to the axis value.

(b) Response C-error for structure subsystem reduction using all eigenvectors with associated frequency less than or equal to the axis value.

(c) Dam crest relative horizontal displacement for a ROM that uses 20% of the eigenvectors of the structure and the fluid.

Fig. 20. Performance of ROM using the model of Fig. 19. C-errors are calculated with respect to the DFMT-CFA benchmark results.
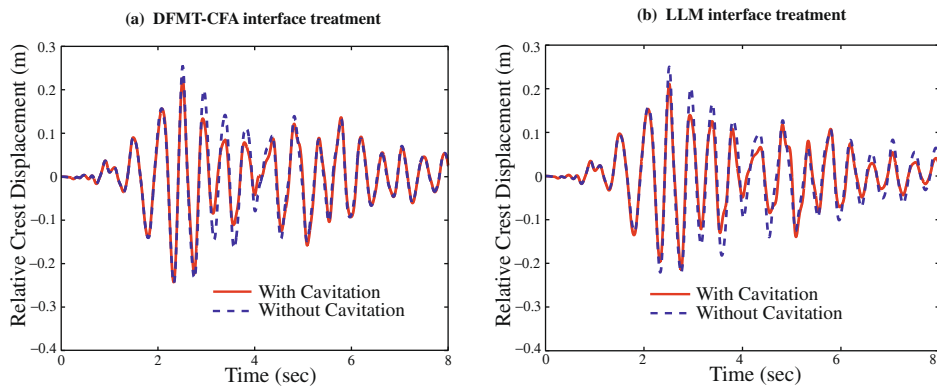
Fig. 21. Dam crest relative horizontal displacement histories calculated with (a) DFMT-CFA and (b) LLM interface treatments, with and without cavitation effects admitted.
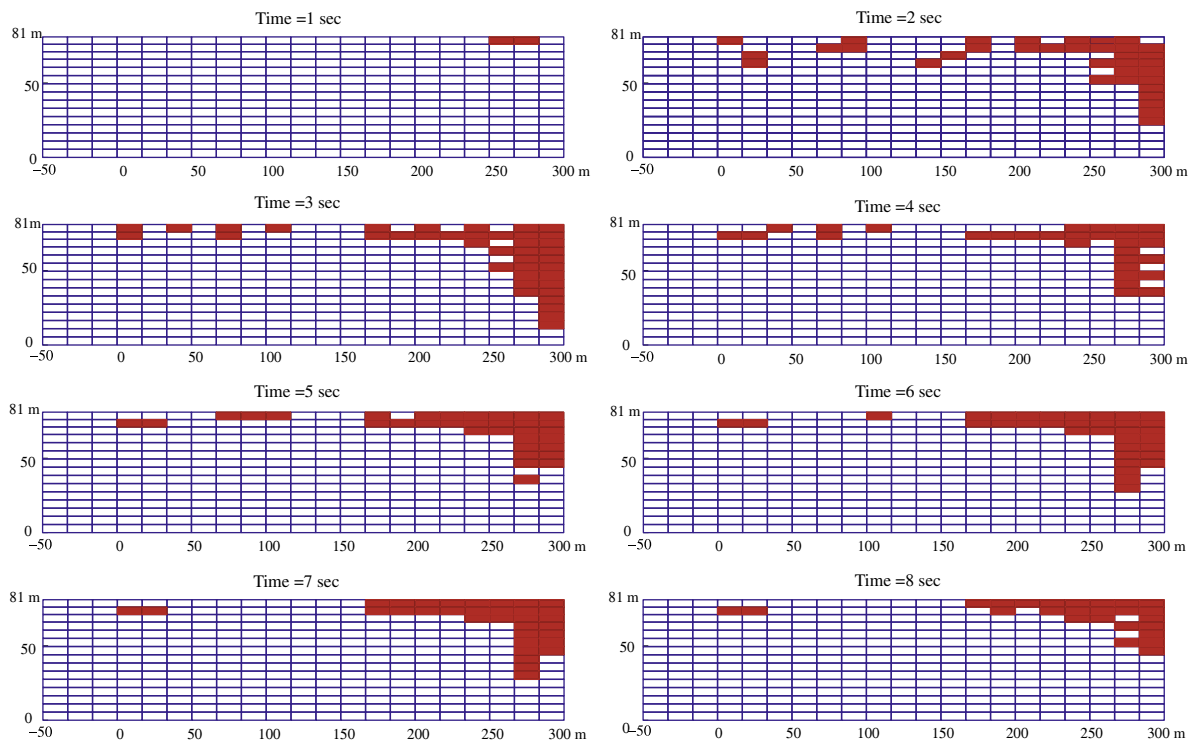
Fig. 22. Snapshots of cavitation regions calculated with LLM interface coupling; cavitating elements are filled. The dam face is located at 300 m.

in Fig. 20c, shows excellent agreement with the benchmark response.

4.5.6. Cavitation effects

We now present selected results for the transient-response analysis of the Koyna Dam accounting for cavitation effects. To trigger significant cavitation, it was found necessary to scale the El Centro horizontal acceleration data so the maximum horizontal acceleration reaches approximately 1.5 g. Both the LLM and DFMT-CFA interface treatments were used, where both employed central-difference time integration for the fluid as discussed in Section 4.4. In both cases frothing is suppressed by injection of numerical damping in the fluid. The DFMT-CFA treatment employs artificial damping as described in [15,36] with coefficient of $\beta = 0.25$, whereas LLM treatment employs Rayleigh damping of the form $\mathbf{C}_{Fd} = \alpha_K \mathbf{K}_{Fd} + \alpha_M \mathbf{M}_{Fd}$ with $\alpha_K = 10^{-3}$ and $\alpha_M = 0$.

Fig. 21 compares dam-crest displacement histories (relative to the base displacement) obtained with the two methods, with and without cavitation admitted. The methods provide similar results; in fact, by tuning the artificial damping parameters the two could produce nearly identical displacement histories. Evolution of the cavitation zone over the 8 s timespan is shown for the LLM calculations in Fig. 22 with snapshots taken at one-second intervals. The event sequence as displayed is physically reasonable, since cavita-

tion starts near the dam wet face and near the free surface, where the hydrostatic pressure is lowest, and propagates upstream as guided by the rarefaction shock.

It can be seen that the LLM and DFMT-CFA treatments produce similar results. However, the use of the central-difference time-integrator for the fluid limits the stable step size. This implies that, assuming the same time stepsize, the LLM interface treatment is more computationally expensive, because of the additional cost in solving the interface equations.

4.6. 3D transient analyses: Morrow point arch dam

This section addresses the application of the LLM interfacing method to a 3D problem with either matching or non-matching meshes on a curved surface. The benchmark problem is the Morrow Point arch dam, pictured in Fig. 23a–c, which has been extensively studied in the literature [11,25,37]. The main focus of the section is the formation of the interface connection matrices on the curved surface of the dam–fluid interface.

A detailed model description of the dam can be found in [34]. The FE model is shown Fig. 24a. As input excitation, we selected the Taft earthquake (Kern County, 21 July 1952) as recorded in the COSMOS database [1]. The largest acceleration data is applied in the horizontal downstream direction. Its acceleration and power

(a) Downstream photo

(b) Modeled portion (rock is assumed rigid; fluid not shown)

(c) Dam cross sections
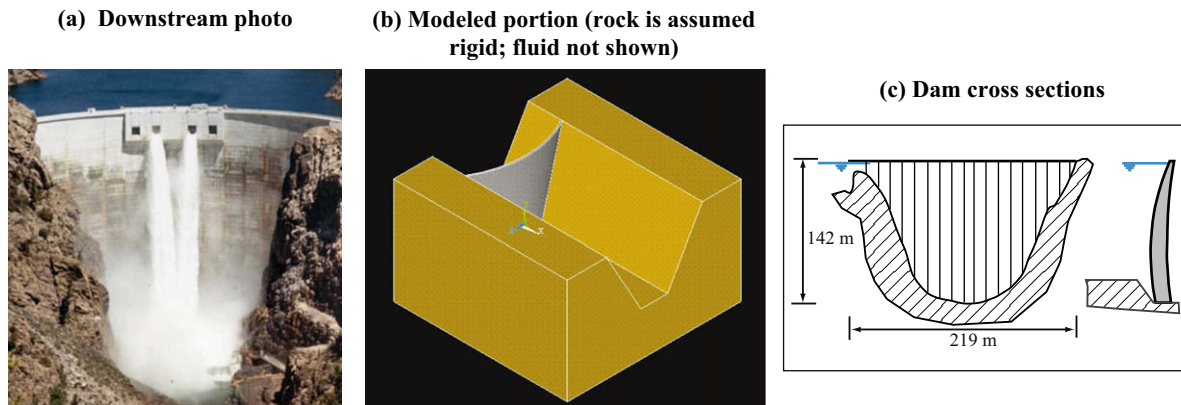
Fig. 23. The Morrow Point arch dam: (a) photograph (taken from <http://www.nps.gov/cure/historyculture/aspinall_unit.htm>), (b) modeled portion, and (c) cross sections [11].

(a) FE structure model and key dimensions

(b) Normal-to-dam horizontal excitation
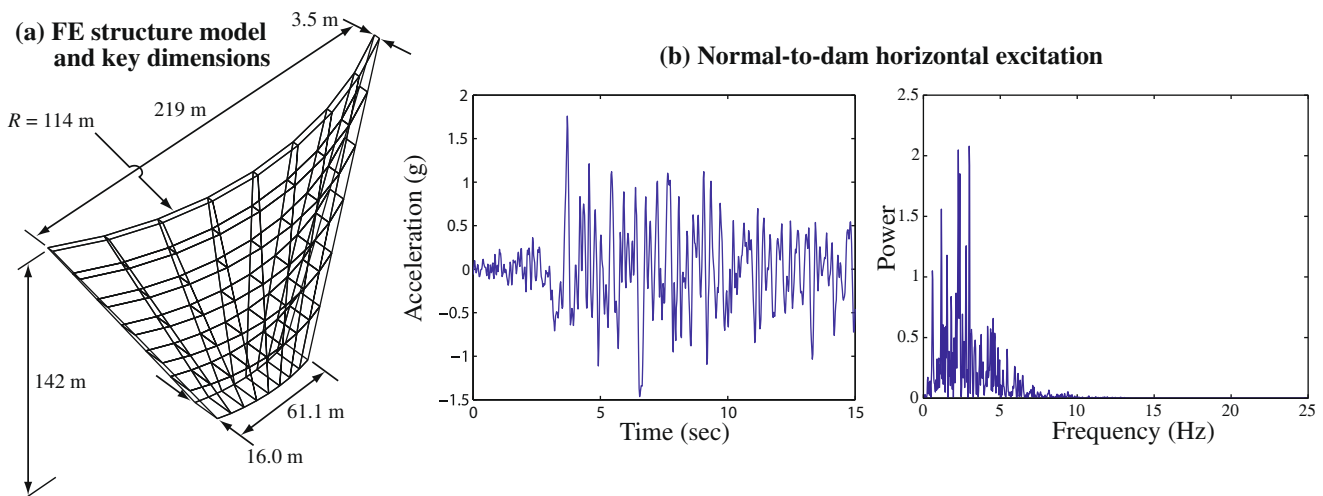
Fig. 24. The Morrow Point dam: (a) dimensions and (b) seismic excitation taken from the 1952 Taft earthquake [1].
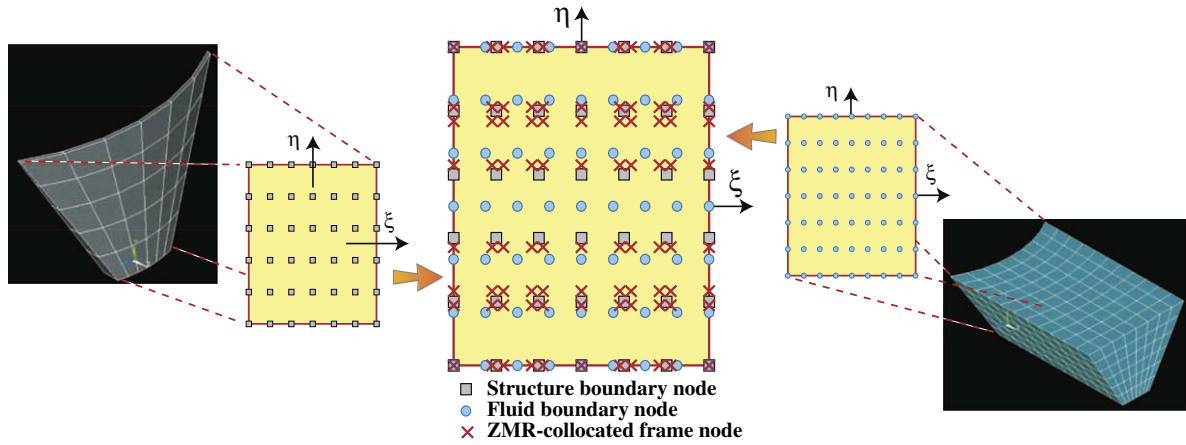
Fig. 25. Morrow Point dam: isoparametric interface mapping used to construct a ZMR-conforming frame.
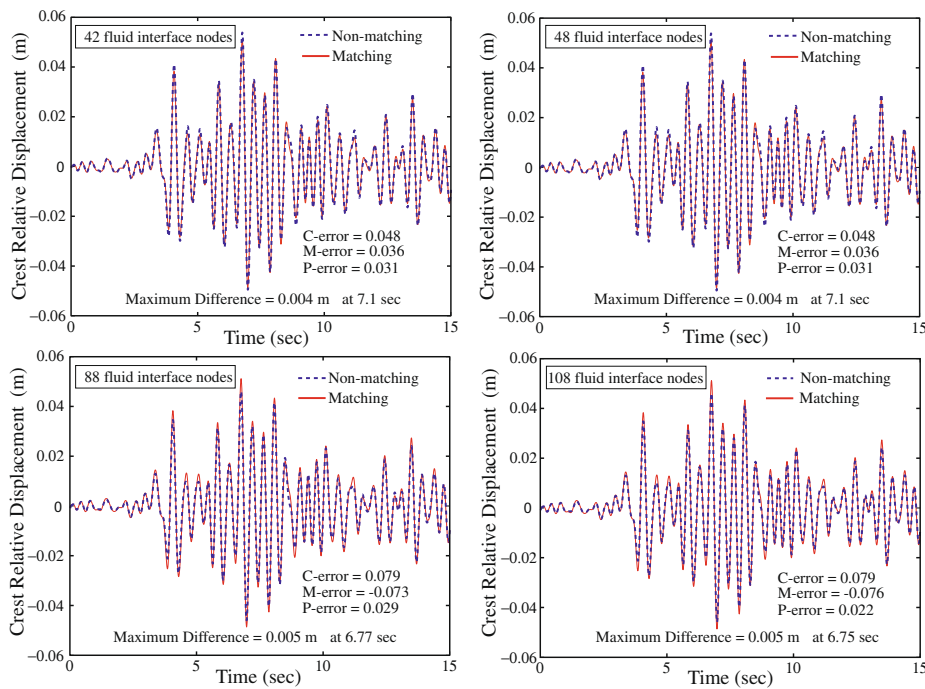
Fig. 26. Dam crest relative-displacement histories calculated with matching and non-matching meshes with 63 structure interface nodes. C-errors are calculated for histories calculated with non-matching meshes relative to that calculated with a matching mesh.

spectrum are shown in Fig. 24b. The other two components are applied in the vertical and cross-stream directions. Unconventionally, a one element thick model was used. The one element thick model is not recommended for an analysis of the dam; however, it was sufficient to illustrate that the LLM method will work on a curved surface using the process discussed next.

4.6.1. Interface connection matrices

The generalization of the ZMR to arbitrary non-matching meshes in 3D connected by delta-function multiplier spaces and a LLM frame remains an open problem. The ZMR can be readily used, however, when the interface surface is rectangular and plane, and element boundary faces are aligned plane rectangles. If so, the rule is applied in tensor product form along each rectangular direction. Frame elements are taken to be 4-node bilinear elements.

This simple recipe can be extended to curved surfaces and regular meshes that can be mapped onto plane rectangles by isoparametric mapping. This is applicable to our Morrow Point dam model since both the structure and fluid volume meshes are fairly regular. The mapping process is illustrated in Fig. 25, for the case where structure and fluid boundary meshes have 6×5 and 8×6 elements, respectively. Frame nodes determined by applying the ZMR along the ξ and η natural directions are subsequently mapped back onto the curved interface.

Although the foregoing process appears intricate, the advantage of constructing a ZMR-conforming frame is the likelihood of having well conditioned interface equations as well as satisfying *a priori* interface-energy conservation. Should the process become too involved for more complicated interface geometries or meshes, there is always the possibility of picking one face as master to collocate LLM frame nodes, or using Mortar or DFMT-CCI. The recommenda-

tions of Section 4.5.2 in regard to master-face selection should be kept in mind.

4.6.2. Response calculations

The transient-response analyses follow the same process used in the Koyna dam analyses, as described in Section 4.5.3. First, a benchmark solution was obtained over a timespan of 15 s with matching meshes by refining the model in both space and time until the relative crest response did not change to plot accuracy.

The fluid mesh was then modified so that non-matching meshes occurred at the interface, and the computed responses were compared to the converged benchmark response. The LLM scheme with the tensor product form of the ZMR illustrated in Fig. 25 was used to treat the interaction. Fig. 26 shows four responses in which the number of fluid nodes at the interface indicates the degree of *non-matching*. The structure has 63 interface nodes whereas the fluid ranges from 42 to 108 interface nodes. The maximum difference between the converged benchmark and the non-matched simulation over the simulated timespan is is noted in the figure, as well as the C-error measure. As can be seen, there is little difference between the matched and non-matched results.

5. Conclusions

The main objective of the paper is to apply the formulation of Localized Lagrange multipliers of the prequel paper [35] to the simulation of actual structures experiencing significant FSI effects, using 2D and 3D models. In addition, several theoretical and implementation issues left out of [35] because of space reasons, are reviewed and explained in further detail. The additional theory topics include procedures for reduced-order modeling and a detailed look at the interface treatment by competing dual methods. In addition to the LLM method, attention is focused on the point-force Mortar and several direct force–motion transfer (DFMT) methods. To our knowledge, this is the first study that compares such a wide range of interfacing techniques, and considers their relative merits as well as equivalence under certain choices of multiplier spaces. Of the methods investigated, the LLM with the zero-moment rule is the only method to possess all of the following desirable attributes:

(1) Passes force and displacement interface patch tests.
(2) Satisfies interface energy conservation conditions.
(3) Maintains full locality of separate meshes.
(4) Provides an error measure for transient analysis.
(5) Properly handles crossing interfaces.

However, the LLM is one of the most complex methods considered in the study.

A 2D problem was used to validate the LLM-coupling of an acoustic fluid to a rigid structure with prescribed displacements. It was also found that truncating the unbounded fluid domain with a PWA boundary and adding artificial damping significantly improved fluid calculations. A 1D problem was used to validate the treatment of cavitation. Because of the small temporal and spatial scales associated with cavitation, an explicit time-integrator must be used for the fluid. Coupled with an implicit time-integrator for the structure, and in the absence of time-step subcycling, calculations with the LLM can become costly.

Vibration and transient analyses were performed with a 2D plane-strain model of the Koyna gravity dam. Vibration analyses with a focus on kinematic continuity at the fluid–structure interfaces provided relatively simple selection guidelines for each interface method as follows:

(1) If using point-force Mortar, choose the refined mesh as master.
(2) If using DFMT-CCI, interpolate from the coarse mesh.
(3) If using LLM, collocate frame nodes as per the ZMR or (if that is too demanding) from the coarse mesh. Avoid frame node collocation at refined mesh nodes.

Transient analyses of the Koyna dam explored a comprehensive range of non-matching mesh interface treatments, including LLM, Mortar and various forms of DFMT coupling. The principle discovery was that if the zero-moment rule is not used with the LLM method or the DFMT-LLM coupling method, there is potential for the occurrence of ill-conditioned interface equations, or energy conservation violations. A simple reduced-order model (ROM) formulation was tested using a subset of the fluid and structure uncoupled eigenmodes. Transient analysis results showed that this choice, when combined with the LLM treatment, to be highly effective.

The nonlinear effect of fluid cavitation was briefly studied on the Koyna dam problem. While cavitation had little effect on the structure response, the primary conclusion is that the DFMT-LLM scheme appears to be the most effective one in the case of non-matching meshes. Further studies on the performance of other combinations on handling nonlinear behavior in the fluid, structure or both, remain subject of further research.

The paper concludes with the 3D simulations of the Morrow Point arch dam. Because of the higher computational and model preparation costs, this analysis was limited to assessing the effectiveness of the LLM interface treatment of a curved interaction surface on the transient response to an actual earthquake. A matched-mesh converged solution was obtained by space-time refinement. For non-matching meshes, a ZMR-conforming frame was constructed by appropriate isoparametric mapping and used in conjunction with the LLM interface treatment. Results showed satisfactory agreement with the converged solutions.

References

[1] Anonymous, COSMOS Virtual Data Center for Strong Motion, Consortium of Organizations for Strong Motion Observation Systems (COSMOS), Pacific Earthquake Engineering Research Center. <http://db.cosmos-eq.org, University of California, Berkeley>.
[2] S.N. Atluri, On "hybrid" finite-element models in solid mechanics, in: R. Vichnevetsky (Ed.), Advances in Computer Methods for Partial Differential Equations, AICA, Rutgers University, 1975, pp. 346–356.
[3] F. Baaijens, A fictitious domain/mortar element method for fluid–structure interaction, Int. J. Numer. Methods Fluid 35 (2001) 743–761.
[4] F. Belgacem, The Mortar finite element method with Lagrange multipliers, Numer. Math. 84 (1999) 173–197.
[5] C. Bernardi, Y. Maday, A.T. Patera, A New Nonconforming Approach to Domain Decomposition: The Mortar Element Method, Technical Report, Université Pierre at Marie Curie, Paris, France, 1990.
[6] H.H. Bleich, I.S. Sandler, Interaction between structures and bilinear fluids, Int. J. Solid Struct. 6 (1970) 617–639.
[7] A.K. Chopra, Hydrodynamic Pressures on Dams During Earthquakes, J. Engrg. Mech. Div. ASCE, 93/EM6, 1967.
[8] A.K. Chopra, P. Chakrabarti, Earthquake analysis of concrete gravity dams including dam–water–foundation rock interaction, Earthq. Engrg. Struct. Dyn. 9 (1981) 363–383.

[9] R.W. Clough, C. Chu-Han, Seismic cavitation effects on gravity dams, in: R.W. Lewis et al. (Eds.), Numerical Methods in Coupled Problems, Wiley, New York, 1984.

[10] B. El-Aidi, Nonlinear Earthquake Response of Concrete Gravity Dam Systems, Ph.D. thesis, California Institute of Technology, Pasadena, 1989.

[11] Z. Duron, J. Hall, Experimental and finite element studies of the forced vibration response of Morrow Point dam, Earthq. Engrg. Struct. Dyn. 16 (1988) 1021–1039.

[12] C. Farhat, M. Lesoinne, N. Maman, Mixed explicit/implicit time integration of coupled aeroelastic problems: three-field formulation, geometric conservation and distributed solution, Int. J. Numer. Methods Engrg. 21 (1995) 807–835.

[13] C. Farhat, S. Piperno, B. Larrouturu, Partitioned procedures for the transient solution of coupled aeroelastic problems; Part I: model problem, theory and two-dimensional application, Comput. Methods Appl. Mech. Engrg. 124 (1995) 79–112.

[14] V. Faucher, A. Combescure, A time and space mortar method for coupling linear modal subdomains and non-linear subdomains in explicit structural dynamics, Comput. Methods Appl. Mech. Engrg. 192 (2003) 509–533.

[15] C.A. Felippa, J.A. DeRuntz, Finite element analysis of shock-induced hull cavitation, Comput. Methods Appl. Mech. Engrg. 44 (1984) 297–337.

[16] T.L. Geers, An objective error measured for the comparison of calculated and measure transient response histories, Shock Vibr. Bull. 54 (1984) 303–316.

[17] S. Hartmann, S. Brunssen, E. Ramm, B. Wohlmuth, Unilateral non-linear dynamic contact of thin-walled structures using a primal-dual active set strategy, Int. J. Numer. Methods Engrg. 70 (2007) 883–912.

[18] B. Herry, L. Di Valentin, A. Combescure, An approach to the connection between subdomains with nonmatching meshes for transient mechanical analysis, Int. J. Numer. Methods Engrg. 55 (2002) 973–1003.

[19] S. Hüeber, B. Wohlmuth, A primal-dual active set strategy for non-linear multibody contact problems, Comput. Methods Appl. Mech. Engrg. 194 (2005) 3147–3166.

[20] L.A. Jakobsen, A Finite Element Approach to Analysis and Sensitivity Analysis of Time Dependent Fluid–Structure Interaction Systems, Ph.D. Dissertation, Aalborg University, Denmark, 2002.

[21] D. Kincaid, W. Cheney, Numerical Analysis: Mathematics of Scientific Computing, Brooks Coleman, 2002.

[22] J. Lysmer, R.L. Kuhlemeyer, Finite dynamic model for infinite media, J. Engrg. Mech. Div. ASCE 95(EM4) (1969) 859–876. August.

[23] R.E. Newton, Finite Element Analysis of Shock-induced Cavitation, Preprint 80-110, ASCE Spring Convention, 1980.

[24] A. Niwa, R.W. Clough, Non-linear seismic response of arch dams, Earthq. Engrg. Struct. Dyn. 10 (1982) 267–281.

[25] C. Noble, Seismic Analysis of Morrow Point Dam, Technical Report UCRL-JC-147993, Lawrence Livermore National Laboratory, April 2002.

[26] B. Parlett, The Symmetric Eigenvalue Problem, Prentice-Hall, Englewood Cliffs, NJ, 1980.

[27] K.C. Park, C.A. Felippa, J.A. DeRuntz, Stabilization of staggered solution procedures for fluid–structure interaction analysis, in: T. Belytschko, T.L. Geers (Eds.), Computational Methods for Fluid–Structure Interaction Problems AMD, vol. 26, American Society of Mechanical Engineers, ASME, New York, 1977, pp. 95–124.

[28] K.C. Park, C.A. Felippa, G. Rebel, A simple algorithm for localized construction of nonmatching structural interfaces, Int. J. Numer. Methods Engrg. 53 (2002) 2117–2142.

[29] K.C. Park, C.A. Felippa, G. Rebel, Interfacing nonmatching finite element discretizations: the Zero Moment Rule, in: W.A. Wall et al. (Eds.), Trends in Computational Mechanics, CIMNE, Barcelona, Spain, 2001, pp. 355–367.

[30] T.H.H. Pian, P. Tong, Basis of finite element methods for solid continua, Int. J. Numer. Methods Engrg. 1 (3) (1969) 29.

[31] W. Prager, Variational principles for linear elastostatics for discontinuous displacements, strains and stresses, in: B. Broger et al. (Eds.), Recent Progress in Applied Mechanics, The Folke-Odgvist Volume, Almqusit and Wiksell, Stockholm, 1967, pp. 463–474.

[32] C.R. Rao, S.K. Mitra, Generalized Inverse of Matrices and its Applications, Wiley, New York, 1971.

[33] J. Rommes, Methods for Eigenvalue Problems with Applications in Model Order Reduction, Ph.D. Dissertation, Utrecht University, 2007.

[34] M.R. Ross, Coupling and simulation of acoustic fluid–structure interaction systems using localized Lagrange multipliers, Ph.D. Dissertation, University of Colorado at Boulder, 2006. <http://caswww.colorado.edu/courses/FSI.d>.

[35] M.R. Ross, C.A. Felippa, K.C. Park, M.A. Sprague, Treatment of acoustic fluid–structure interaction by localized Lagrange multipliers: Formulation, Comput. Methods Appl. Mech. Engrg. 197 (2008) 3057–3079.

[36] M.A. Sprague, T.L. Geers, A spectral-element method for modeling cavitation in transient fluid–structure interaction, Int. J. Numer. Methods Engrg. 60 (2004) 2467–2499.

[37] H. Tan, A. Chopra, Dam-foundation rock interaction effects in earthquake response of arch dams, J. Struct. Engrg. (1996) 528–538.

[38] J. Wilcoski et al., Seismic Testing of a 1/20 Scale Model of Koyna Dam, US Army Corps of Engineers ERDC, Technical Report TR-01-17, November 2001.

[39] B. Wohlmuth, Hierarchical a posteriori error estimators for mortar finite element methods, SIAM J. Numer. Anal. 36 (1999) 1636–1658.

[40] B. Wohlmuth, A mortar finite element method using dual spaces for the Lagrange multipliers, SIAM J. Numer. Anal. 38 (2000) 989–1012.

[41] O.C. Zienkiewicz, D.K. Paul, E. Hinton, Cavitation in fluid–structure response (with particular reference to dams under earthquake loading), Earthq. Engrg. Struct. Dyn. 11 (1983) 463–481.